

Development of a new generation of quench and partitioning steels

Influence of processing parameters on texture, nanoindentation, and mechanical properties

Ariza-Echeverri, E. A.; Masoumi, M.; Nishikawa, A. S.; Mesa, D. H.; Marquez-Rossy, A. E.; Tschiptschin, A. P.

DOI

[10.1016/j.matdes.2019.108329](https://doi.org/10.1016/j.matdes.2019.108329)

Publication date

2020

Document Version

Final published version

Published in

Materials and Design

Citation (APA)

Ariza-Echeverri, E. A., Masoumi, M., Nishikawa, A. S., Mesa, D. H., Marquez-Rossy, A. E., & Tschiptschin, A. P. (2020). Development of a new generation of quench and partitioning steels: Influence of processing parameters on texture, nanoindentation, and mechanical properties. *Materials and Design*, 186, Article 108329. <https://doi.org/10.1016/j.matdes.2019.108329>

Important note

To cite this publication, please use the final published version (if applicable).
Please check the document version above.

Copyright

Other than for strictly personal use, it is not permitted to download, forward or distribute the text or part of it, without the consent of the author(s) and/or copyright holder(s), unless the work is under an open content license such as Creative Commons.

Takedown policy

Please contact us and provide details if you believe this document breaches copyrights.
We will remove access to the work immediately and investigate your claim.



Development of a new generation of quench and partitioning steels: Influence of processing parameters on texture, nanoindentation, and mechanical properties

E.A. Ariza-Echeverri ^{a,*}, M. Masoumi ^b, A.S. Nishikawa ^{a,c}, D.H. Mesa ^d, A.E. Marquez-Rossy ^e, A.P. Tschiptschin ^a

^a Department of Metallurgical and Materials Engineering, University of São Paulo, Av. Prof. Mello Moraes, 2463, CEP 05508-030 São Paulo, SP, Brazil

^b Federal University of ABC, Center of Engineering, Modelling and Applied Social Sciences, Bangú, 09210-580 Santo André, SP, Brazil

^c Department of Materials Science and Engineering, Delft University of Technology, Mekelweg 2, Delft 2628 CD, the Netherlands

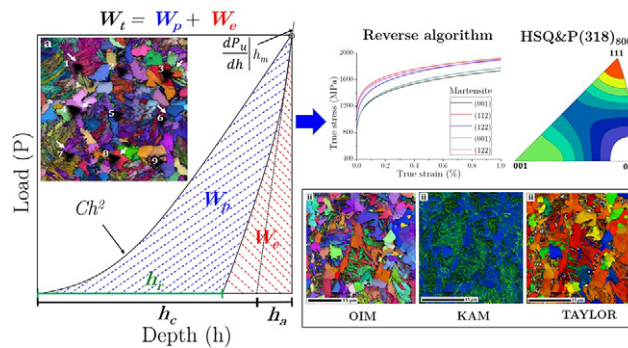
^d Mechanical Technology Program, Universidad Tecnológica de Pereira, Vereda La Julita, Pereira, Risaralda, Colombia

^e Deposition Science and Technology Group, Oak Ridge National Laboratory, Oak Ridge, TN 37830, USA

HIGHLIGHTS

- Hot stamping followed by Q&P process in TRIP-steels causes excellent combination of mechanical strength and elongation
- Combined nanoindentation and EBSD analysis is applied for phase identification and calculate localized mechanical properties
- Predominance of {110}//ND texture in retained austenite grains
- {111} and {112}//ND texture in BCC grains enhances efficiently the TRIP-effect.

GRAPHICAL ABSTRACT



ARTICLE INFO

Article history:

Received 9 June 2019

Received in revised form 24 October 2019

Accepted 4 November 2019

Available online 6 November 2019

Keywords:

Nanoindentation

EBSD

TRIP-steel

Crystallographic texture

Subsize tensile test

ABSTRACT

A novel quenching and partitioning process (Q&P) including the hot stamping (HS) process was studied, using two stamping temperatures (750 °C and 800 °C) and two quenching temperatures (318 °C and 328 °C). This combination is here called Hot Stamping and Quenching and Partitioning process (HSQ&P). The partitioning step was performed at 400 °C for 100 s in all cycles. Microstructural features were comprehensively studied using electron backscattered diffraction and nanoindentation techniques. HSQ&P samples showed a good combination of ductility and high-strength due to the presence of: retained austenite, inter-critical ferrite with low stored internal strain energy, grain refinement via DIFT-effect (deformation induced ferrite transformation), martensite, and bainite. Significant internal stress relief was caused by carbon partitioning, which was induced by the DIFT-effect and the partitioning stage. This also led to a considerable stored energy, which was characterized by the Kernel average dislocation and geometrically necessary dislocation analysis. In addition, predominant {110}//strain direction crystallographic texture was identified, which promotes slip deformation and enhances the mechanical properties. Moreover, remarkable amounts of fine film-like retained austenite oriented

* Corresponding author.

E-mail address: andersonariza@usp.br (E.A. Ariza-Echeverri).

along compact crystallographic directions (i.e., $\langle 111 \rangle$ and $\langle 112 \rangle$) were observed. Finally, subsize tensile test verified the optimum mechanical behavior of HSQ&P specimens.

© 2019 Published by Elsevier Ltd. This is an open access article under the CC BY-NC-ND license (<http://creativecommons.org/licenses/by-nc-nd/4.0/>).

1. Introduction

The automotive industry has a great interest in a new generation of steels containing i) considerable amount of retained austenite stabilized at room temperature to increase ductility, ii) low carbon content to ease weldability, and iii) low contents of alloying elements to reduce material cost [1–4]. Quenching and partitioning (Q&P) process, proposed by Speer et al. [5], has been used to attain these characteristics. The main objective of the Q&P process is to produce a ferritic-martensitic microstructure with controlled fractions of retained austenite stabilized by the carbon partitioning from martensite. The retained austenite enhances the mechanical properties by increasing the ductility and toughness of the material due to the transformation induced plasticity (TRIP) effect. The Q&P process starts with heating the steel to an austenitizing temperature above the A_{c3} or between the A_{c1} and A_{c3} to ensure full or partial austenitization, respectively. The steel is maintained at this temperature for a time determined by the part size. The austenitization step is followed by the rapid cooling (quenching) to a quenching temperature between the martensite start and finish transformation temperatures (M_s and M_f), to produce a controlled fraction of carbon-saturated martensite. Next, a partitioning step is conducted by either maintaining the temperature at the quenching temperature for a longer time (one-step Q&P) or by increasing the temperature (two-step Q&P) to what is called partitioning temperature close to the M_s . Finally, the material is quenched to room temperature. The goal of the partitioning step is to promote the migration of the carbon atoms (partitioning) from the carbon-saturated martensite to the untransformed austenite. Although the production of carbon-depleted martensite and carbon-enriched retained austenite is the main goal of Q&P process, bainitic-ferrite can also be formed during the partitioning stage, and fresh martensite may be transformed from insufficiently carbon-enriched austenite during the last quenching step. The partitioning process increases the stability of the untransformed austenite at room temperature by minimizing or fully suppressing the transformation of the austenite to fresh martensite during the final quenching step [6–8].

In order to improve ductility without compromising strength, the Q&P process is currently being integrated into the thermo-mechanical controlled processing (TMCP), such as hot rolling [9–12], hot compression [13,14], Deformation Induced Ferrite Transformation (DIFT) technology [15,16], and hot stamping (HS) or die quenching [17–22]. Hot stamping consists in the deformation of the steel in the range 900 °C–800 °C, followed by rapid cooling in the mold, in order to obtain a fully martensitic microstructure, which shows a limited room temperature elongation [23]. The advantage of the hot stamping process is the simultaneous improvement of the mechanical strength due to the refinement of the microstructure, and the suppression of the springback effect. Complex TMCP+Q&P cycles encompass a high number of parameters, which can modify the microstructure and the mechanical properties at room temperature. These parameters include: (i) austenitizing temperature (full or partial); (ii) isothermal [13–16,19] and non-isothermal [10–12,20,21] deformation at high temperatures, and; (iii) Q&P process, involving rapid cooling rates to optimum quenching temperature (OQT), in order to maximize the retained austenite fraction after the final cooling [24]. The OQT in turn can be affected by the previous hot deformation, which has not been accurately studied in the literature. Additionally, as already mentioned, the Q&P process can be

carried out in one or two-step, but in one-step is the most commonly used process [10,11,17,18,20] due to the greater facility of its industrial implementation. However, more complex processes such as HS+Q&P in two-step have also been explored [9,11,12,19,25] due a more favor kinetics of carbon partitioning. It is important to highlight that the quenching and partitioning times are also determined in the Q&P treatments. Although the addition of Si, Mn, and Al in the composition can retard the carbide precipitation, the times at the OQT should be kept short (5–10 s) to reduce the precipitation and coarsening of carbides [26]. However, completely avoiding secondary precipitation is challenging since the formation of ϵ and η transition carbides has been reported both during quenching and short isothermal soaking times [27–29]. Also, for excessive soaking periods, these transition carbides can transform to cementite inside martensite and retained austenite [27,30]. However, the few studies that have been carried out on the HS+Q&P in two steps, have used very long holding times (>1 min) at the initial quenching step [12,19]. Recently, Zhu et al. [31] and Wang et al. [22] proposed an innovative approach involving a two-step Q&P combined with a hot stamping process; however, as the mold was maintained at 280 °C, their results are arguable, since the cooling rates employed throughout the thermal process are not fast enough to guarantee the occurrence of martensitic transformation.

Additionally, most of the mentioned studies were focused mainly on fully austenitized samples [10–13,16,19–22]. However, this process could be improved by the use of inter-critical annealing temperatures, to obtain inter-critical ferrite, higher carbon contents in austenite (>2 wt%), and higher hardenability in such a way that the Q&P process could be applied without ferrite precipitation during cooling [32]. On the other hand, non-isothermal deformations at high temperature can induce the formation of DIFT ferrite [33]. Hence, the formation of both ferrites (inter-critical and DIFT) can favor the increase of the ductility of the material. Likewise, most of the researches combining HS and Q&P processes focused on boron steels [13,17,18,20,21] because they are the most used steels in the HS process, disregarding the potential of other advanced high strength steels, such as TRIP-steel. In general, the previously mentioned studies combining TMCP and Q&P clearly showed the resulting properties related with variations in austenite stability or grain size refinements; however, the influence of the distribution of localized plastic deformation in the grain scale, the evolution of texture, and phase identification by combining EBSD and nanoindentation, and their effect on mechanical performance, have received limited attention.

In this research, we propose a comprehensive approach to understand the critical stages of a complex thermomechanical process, in order to increase the ductility, without compromising strength in a TRIP-assisted steel. Here, we study the effects of non-isothermal and isothermal inter-critical hot stamping, followed by two-step Q&P treatment. The influence of DIFT ferrite, inter-critical ferrite, and retained austenite were also discussed. The main objective of this work is to achieve optimum mechanical properties in TRIP-assisted steel by means of a combination of hot stamping followed by quenching and partitioning (HSQ&P) processes. In this respect, six different thermomechanical paths (two Q&P and four HSQ&P) were applied to a commercial TRIP-assisted steel. A comprehensive study of the obtained microstructures was carried out by using the EBSD technique to help understanding the local mechanical behaviors. Finally, sub-size tensile test was carried out to verify the mechanical results of the proposed HSQ&P process.

2. Material and experimental procedures

A TRIP steel (Fe–0.23C–1.23Si–1.50Mn–0.018P–0.003S, wt%) was subjected to Q&P and HSQ&P thermomechanical treatments using an Advanced Gleeble®3550 thermomechanical simulator. Dog-bone shaped samples with gauge length of 10 mm, width of 5 mm, and thickness of 1.5 mm, were carefully prepared using wire electro-discharge machining along the longitudinal axis parallel to the rolling direction. This specimen was developed by the technical staff of the Nanotechnology National Laboratory in Brazil where the Advanced Gleeble®3550 is installed. Several previous experiments were carried out leading to the selection of the specimen geometry. The samples were homogenized for 5 min at 1000 °C, and then intercritically annealed at 800 °C for 5 min to obtain intercritical ferrite, higher carbon contents in austenite, and higher hardenability, avoiding ferrite precipitation during cooling. Next, two samples were subjected to the Q&P process, by quenching at 318 and 328 °C and partitioning at 400 °C for 100 s, followed by cooling to room temperature. The optimum quenching temperature (318 °C) was calculated according to the constrained carbon equilibrium criterion [5]. The heating rate in all heating steps was 15 °C/s, while the cooling rate was 60 °C/s.

Four samples were subjected to the HSQ&P process. The HSQ&P experiments were studied to clarify whether the DIFT-effect contributes to improve ductility, without compromising strength. After the initial intercritical austenitization step, the samples were strained either isothermally at 800 °C, between $Ac_3 - Ac_1$, (HSQ&P₈₀₀), or non-isothermally, starting about 10 °C below Ac_1 , (HSQ&P₇₅₀). The 750 °C and 800 °C initial deformation temperatures were selected to obtain intercritical and DIFT ferrites, and higher carbon contents in austenite (>2 wt%). The carbon enrichment of the austenite provides higher hardenability, allowing the Q&P process to be applied without ferrite precipitation during cooling, enhancing the stability of the remaining austenite against bainitic transformation. In all conditions the strain was applied at a rate of 0.5 s⁻¹ up to 30%. This strain rate is equivalent to rates used during typical hot stamping process [32]. Thereafter, the samples were quenched at 318 or 328 °C and partitioned at 400 °C for 100 s. The HSQ&P(328)₇₅₀ notation, for example, indicates the sample strained at 750 °C and quenched at 328 °C sample. A non-contact laser dilatometer was used to control the applied strain and to monitor the samples dilation.

In this research, EBSD technique was used to identify microstructural features, in five different regions (five scans) of each sample, as a comprehensive method for understanding the resulting Orientation Image Micrographs (OIMs). In the results, the most representative scan was chosen from the five Orientation Image Maps (OIM). OIM, confidence index (CI), phase identification, and Kernel Average Misorientation (KAM) maps calculated with point-by-point orientation data were used for identification of each microconstituent present in the microstructure.

Electron back-scattered diffraction (EBSD) analyses were conducted in FEI Inspect 50 FE-SEM microscope using acceleration voltage of 20 keV, working distance of 15 mm, specimen tilt angle of 70°, and a scan step size of 100 nm. Nanohardness measurements were carried out on the surface of the samples previously prepared for EBSD analysis using a Triboindenter Hysitron TI 950. The equipment was operated in load control testing mode, with a maximum load of 15 mN. Bergles [34] and Tam [35] claim that indentation size effects (ISE) are recognized to be stronger in the small indentation depth regime and weaken gradually with increasingly deep indentations. Therefore, the aim of using constant and high load values during nanoindentation tests was to reduce the effects associated with the size of the indentation. A nanohardness conversion algorithm for the prediction of mechanical properties was used. A lot of research has been done on the use of methods that make it possible to extract mechanical properties of materials from nanoindentation tests [36–40]. Among them, Dao et al. [39] developed a complete reverse analysis theory to determine the elastic

and plastic properties from load-displacement ($P-h$) curves calculated by nanoindentation. Accordingly, in the present study, to determine the strain-hardening exponent and the yield strength, the algorithm proposed by Dao et al. [39] has been replicated, considering that the plasticity proceeds along a power law hardening:

$$\sigma = \begin{cases} E\varepsilon, & \text{for } \sigma \leq \sigma_y \\ R\varepsilon^n, & \text{for } \sigma \geq \sigma_y \end{cases} \quad (1)$$

where ε is the total effective stress, E is the elastic modulus, σ_y the yield strength, R is a strengthening coefficient, and n is the work-hardening exponent. To resolve the onset of plastic instability, the yield strength can be calculated at the point where the real strain obeys the Considère criterion [41] (i.e., when $\sigma = d\sigma/d\varepsilon$ or $\varepsilon = n$, necking occurs). In addition, for the plastic deformation region ($\sigma \geq \sigma_y$) the Eq. (1) can also be written as a function of the σ_y , plastic strain (ε_p), and E , as:

$$\sigma = \sigma_y \left(1 + \frac{E}{\sigma_y} \varepsilon_p \right)^n \quad (2)$$

Eq. (2) is functional since it enables expressing the σ_y in terms of the elastic-plastic properties of the steel, excluding the requisite of using the R coefficient. Fig. 1 shows a common load-depth of penetration of indenter ($P-h$) curve. During loading progression, the response establishes Kick's law:

$$P = Ch^2 \quad (3)$$

where C is the loading curvature. The average contact pressure, $p_a = \frac{P_m}{A_m}$ (with A_m the projected contact area calculated at the P_m , maximum load applied) can be correlated to the hardness in the indentation regime. The maximum penetration depth, h_m , occurs at P_m , and the unloading slope is differentiated analytically as $\frac{dP_u}{dh}|_{h_m}$, where $P_u = B(h_s - h_r)^m$, where B and m are constants that depend upon the material and the shape of indenter and h_r is the depth of the residual indentation after complete unloading. Hence, C , $\frac{dP_u}{dh}|_{h_m}$, and $\frac{h_r}{h_m}$ are three independent

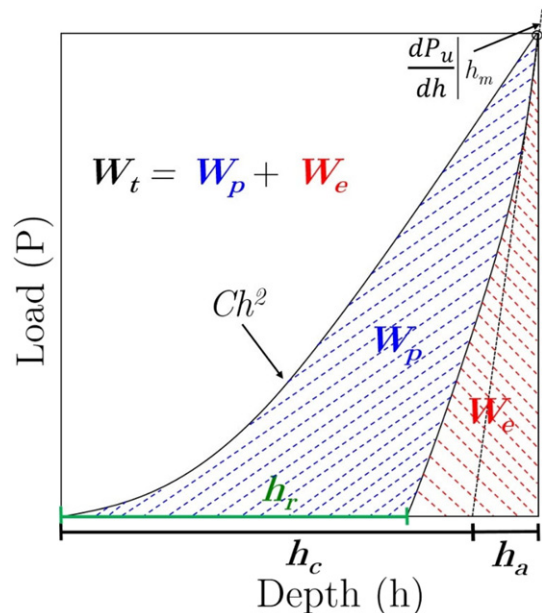


Fig. 1. Schematic representation of a load versus penetration depth curve for instrumented indentation technique.

shape parameters that can be obtained from the $P - h$ curve. It is accepted that the A_m can be calculated disregarding the outcomes of sink in and pile up, as a function of h_m :

$$A_m = c^* h_m^2 \quad (4)$$

where $c^* = 24.56$ for the Berkovich indenter. Based on an energetic approach, W_t is the total work done by load P during loading (found by the integration of Kick's law), W_p is the stored (plastic) work (area under the loading curve or energy dissipation), and W_e is the released (elastic) work during unloading (area under the unloading curve or recovery energy). Hence, the work induced in plastic deformation is $W_p = W_t - W_e$.

The merit of the reverse analysis scheme projected by Dao et al. [39] has taken advantage of dimensionless Π functions to demonstrate a univocal correlation between the shape parameters and the uniaxial mechanical properties. As a first step, the authors expressed the indentation loading response as a function of four variables, h , E^* , σ_r , and n :

$$P = P(h, E^*, \sigma_r, n) \quad (5)$$

where σ_r is a representative real stress corresponding to a representative (arbitrary) strain, and E^* is the reduced Young's modulus due to a non-rigid indenter, which is a combination of the Young's modulus and Poisson's ratio of the specimen and the indenter:

$$E^* = \left[\frac{1-\nu^2}{E} + \frac{1-\nu_i^2}{E_i} \right]^{-1} \quad (6)$$

where E and ν are Young's modulus and Poisson's ratio of the material. The i subscript symbolizes the same properties corresponding to the indenter ($E_i = 1140$ GPa and $\nu_i = 0.07$).

Subsequently, the authors determined a set of dimensionless Π functions correlating the three independent shape parameters calculated from the loading curve (i.e., C , $\frac{dP_u}{dh}|_{h_m}$, and $\frac{h_r}{h_m}$) with the tensile mechanical properties which characterize the stress-strain curve of the specimen (E^* , $\sigma_{0.033}$, n , and p_a). The set of dimensionless Π functions used in this research are shown in the Eqs. (7) to (10). The representative stress, $\sigma_{0.033}$, corresponding to a value of strain of 0.033 was used as a convenient mode to describe Eq. (5) only as a function of $\frac{E^*}{\sigma_{0.033}}$.

$$\Pi_1 = \frac{C}{\sigma_{0.033}} = -1.131 \left[\ln \left(\frac{E^*}{\sigma_{0.033}} \right) \right]^3 + 13.635 \left[\ln \left(\frac{E^*}{\sigma_{0.033}} \right) \right]^2 - 30.594 \left[\ln \left(\frac{E^*}{\sigma_{0.033}} \right) \right] + 29.267 \quad (7)$$

$$\begin{aligned} \Pi_2 \left(\frac{E^*}{\sigma_{0.033}}, n \right) &= \frac{1}{E^* \times h_m} \times \frac{dP_u}{dh} \Big|_{h_m} \\ &= (-1.40557n^3 + 0.77526n^2 + 0.15830n - 0.06831) \\ &\quad \left[\ln \left(\frac{E^*}{\sigma_{0.033}} \right) \right]^3 + (17.93006n^3 - 9.22091n^2 - 2.37733n + 0.86295) \\ &\quad \left[\ln \left(\frac{E^*}{\sigma_{0.033}} \right) \right]^2 + (-79.99715n^3 + 40.55620n^2 + 9.00157n - 2.54543) \\ &\quad \left[\ln \left(\frac{E^*}{\sigma_{0.033}} \right) \right] + (122.65069n^3 - 63.88418n^2 - 9.58936n + 6.20045) \end{aligned} \quad (8)$$

$$\Pi_3 = \frac{p_a}{E^*} = 0.268536 \left(0.9952495 - \frac{h_r}{h_m} \right)^{1.1142735} \quad (9)$$

$$\Pi_4 = \frac{W_p}{W_t} = 1.61217 \left\{ 1.13111 - 1.747756 \left[-1.49291 \left(\frac{h_r}{h_m} \right)^{2.535334} \right] - 0.075187 \left(\frac{h_r}{h_m} \right)^{1.135826} \right\} \quad (10)$$

The Eq. (9) and the dimensionless function Π_4 can be related according to:

$$\frac{p_a}{E^*} = \frac{1}{E^*} \left(\frac{P_m}{A_m} \right) = \Pi_4 \left(\frac{h_r}{h_m} \right) \quad (11)$$

Using the Eqs. (4) and (11), it is possible to solve for A_m and E^* to obtain the average contact pressure, p_a . From the solution of this relation and using the dimensionless function Π_1 it is feasible to determine the representative stress value ($\sigma_{0.033}$). The solution of the Eq. (7) allow by means of adimensional Π_2 to determine the unique solution of the strain hardening exponent, n . Consequently, knowing the value of the Poisson's ratio, ($\nu = 0.3$, for steel), and having determined the value of n , it is possible to obtain the unique solution for σ_y . In this way, the proposed reverse analysis provides a unique solution of the reduced n and σ_y . This means that solving these dimensionless Π functions, and since the elastic properties are known, the yield strength, σ_y , can be inversely determined from Eq. (1). Additionally, subsized tensile specimens with reduced gauge lengths were machined from the central area of the Gleeble samples after the thermomechanical processes. The details of the procedure for obtaining the mechanical properties can be found in [24].

First, the nanoindentation tests were conducted on a $100 \mu\text{m} \times 100 \mu\text{m}$ area, being the indents spaced about $10 \mu\text{m}$ between each other. Then, the EBSD analyses were carried out on the same areas to study the effect of microstructure, crystallographic orientation, and gradients of lattice distortion on the mechanical properties, helping to predict the mechanical behavior of the resulting TRIP steels. In the present study tensile stresses in the SD was assumed for Schmid/Taylor analysis. The grain orientation of tensile samples is presented by a combination of crystallographic plane and direction $\{hkl\}\langle uvw \rangle$, which $\{hkl\}$ planes are parallel to the tensile plane and $\langle uvw \rangle$ directions are parallel to the strain (tensile) direction.

The phase identification was carried out by the correlation of nano-indentation values, image quality (IQ), and Kernel Average Misorientation (KAM). It is well known that the IQ parameter helps in distinguishing the microconstituents by the degree of lattice imperfection. This is because a lattice distorted by crystalline defects such as high dislocation density, lattice strain and grain and/or sub-grain boundaries will have a deformed arrangement of the Kikuchi bands in the back-scattered patterns, lowering IQ values [42,43]. The orientation data acquired by EBSD scan can also be used to investigate the local strain distribution among different grains, which is important to identify the orientation gradients physically associated with dislocation glide and crystal lattice rotation [44,45]. The KAM distribution map represents the arithmetic average misorientation between a point in the center of a pre-determined kernel and the points in the perimeter of the kernel [43]. KAM and Geometrically Necessary Dislocations (GND) provide detailed data about intrinsic stored energy, crystal local strain, and dislocation density. KAM method measures the stored energy based on the average misorientation between one point (reference) and its neighbors and GND estimates dislocation densities located in the interior of the cell and in the cell/sub-grains walls. Thus, KAM was used to qualitatively evaluate small local strain gradients or localized plastic strain distribution among different grains [44]. The characterization of a wide range of ferrites, such as epitaxial, inter-critical, bainitic, DIFT, and martensite from BCC Kikuchi patterns obtained from EBSD technique was carried out by using combination of image quality pattern, KAM, Taylor factor, and local crystal deformation.

3. Results and discussion

3.1. Phase identification using nanoindentation and EBSD

The IQ combined with phase identification was used to distinguish face-centered cubic (FCC) and body-centered cubic (BCC) phases, while IQ combined with KAM (calculated for the 5th nearest neighbor of each point and with upper limit of 10°) was used to distinguish the BCC ferrite and martensite areas. The gray color in Fig. 2a corresponds to the BCC crystal structure, and the red corresponds to FCC phase (retained austenite). It is known that martensite has a higher degree of lattice distortion (tetragonal distortion related to its carbon content [46]) and a larger density of sub-grain boundaries [42]. Hence, the higher values of hardness (ranged from 5.1 to 6.8 GPa) match the darker areas (as shown clearly in yellow ellipses in Fig. 2a), which indicate lower IQ (or band contrast, BC) and high dislocation density. In Fig. 2b, the blue color shows kernel average misorientations $<2^\circ$, green between 2° and 4° , yellow between 4° and 6° , orange between 6° and 8° , and red between 8° and 10° . This figure indicates that the highest values of KAM are present in locations of greater lattice deformation (i.e., martensite areas) and the lowest KAM values correspond to ferrite grains with higher BC (as shown in blue ellipses in Fig. 2a). Consequently, the correlation between high dislocation densities and the low image quality is evident [42], which can be confirmed by high nanohardness values. Accordingly, the differentiation of IQ and KAM distributions caused by the lattice imperfections can be readily used to identify the orientation gradients for discrimination among ferrite and tempered and fresh martensites in the TRIP-assisted steel [26]. Moreover, it is well known that elastic lattice strain should have no effect on IQ and hence its significant variation can be related to the formation of different BCC products.

The quality of the obtained Kikuchi pattern is influenced by the density of defects and dislocations, grain boundaries, lattice strain, and superposition of diffraction patterns from many neighboring crystals [47]. Mechanical polishing can also introduce defects which can directly affect the image quality (IQ) and its effect cannot be disregarded. In areas with low pattern quality due to heterogeneities in sample preparation, the pattern contrast is dominated by noise, leading to significant reduction in IQ index. However, in the present study all samples were

carefully prepared down to colloidal silica to reduce polishing artifacts. In our case, the poor band contrast could be related to complex overlapping patterns, which depend on step size and the depth resolution [48]. Inter-critical ferrite formed between Ac_3 and Ac_1 , during inter-critical annealing, shows the highest confidence quality index due to good compliance of achieved Kikuchi patterns (Fig. 3a and b). In contrast, tempered martensite (α') and fresh martensite (α'_f) have the least conformity quality index because of the high dislocation density and the crystallographic distortion caused by the tetragonality induced by the carbon content trapped in their lattice. Moreover, the α'_f grains are smaller than the α' grains formed during the first quenching process, because they transform from smaller unstable austenite regions after the partitioning process. On the other hand, carbon enrichment of austenite during the partitioning step leads to an increase of its lattice parameter and dislocation density. Zhang et al. [49] reported that the minimum carbon content required to austenite stabilization is 1 wt%. However, only the austenite with a carbon content <1.5 wt% can effectively contribute to the TRIP effect [10].

Fine inter-critical ferrite grains ($<3 \mu\text{m}$ [33]) can be identified by low KAM values in Fig. 3d. These grains are generated at the inter-critical temperature (proeutectoid ferrite) and under stamping conditions, by deformation induced ferrite transformation effect (DIFT- α). Thermodynamically, in the DIFT effect the stored deformation energy in austenite increases the driving force for phase transformation [50]. Under deformation conditions, the driving force depends on two energy components, one is the chemical free energy and the other is the stored deformation energy. This excess energy can induce or accelerate the austenite to ferrite transformation at temperatures above the Ae_1 or Ae_3 temperatures [51]. This means that after deformation of the austenite, at a certain temperature, the Gibbs free energy of austenite increases because of the stored deformation energy. Therefore, although the hot stamping at 750°C may produce new shear bands, sub-grains boundaries, and interfaces, it can also provide additional driving force to form DIFT-ferrite. Since DIFT- α grains nucleate at prior austenite grain boundaries at the early stages of the phase transformation, austenite/ferrite interface can gradually grow under stamping conditions. Hence, the deformation at the inter-critical temperature increases the γ/α interface mobility, rejecting more carbon atoms from newly formed

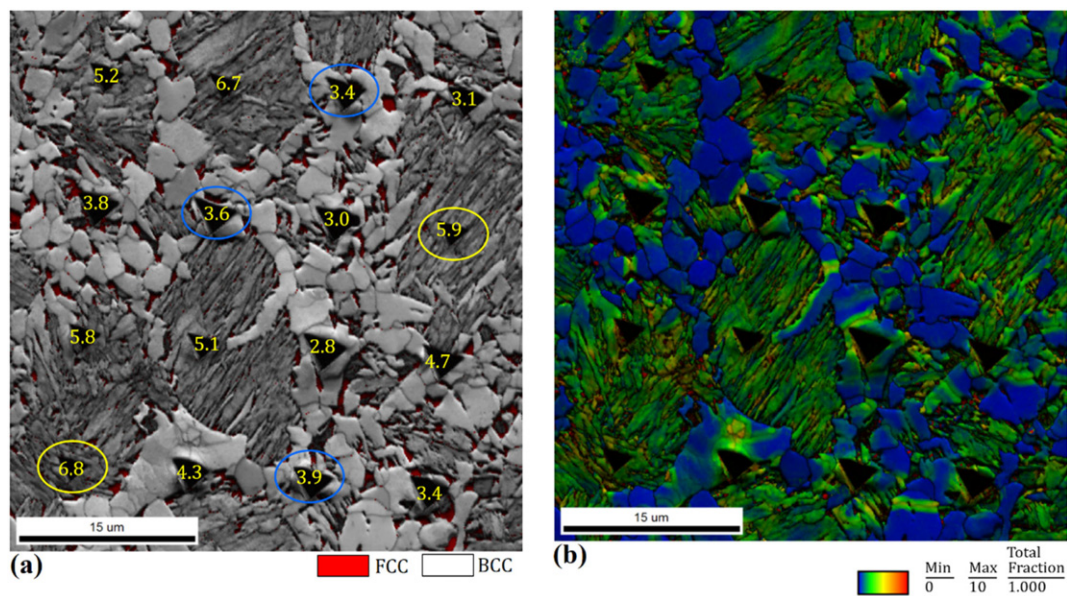


Fig. 2. Identification of phases by nanoindentation, image quality (IQ), and kernel average misorientation (KAM) in the HSQ&P₈₀₀ processed TRIP-assisted steel. (a) Combined IQ map and color-coded phase map. Blue and yellow ellipses indicate ferrite and martensite regions, respectively. (b) KAM map calculated with the 5th nearest neighbor of each point and upper limit of 10° . Nanohardness values in GPa.

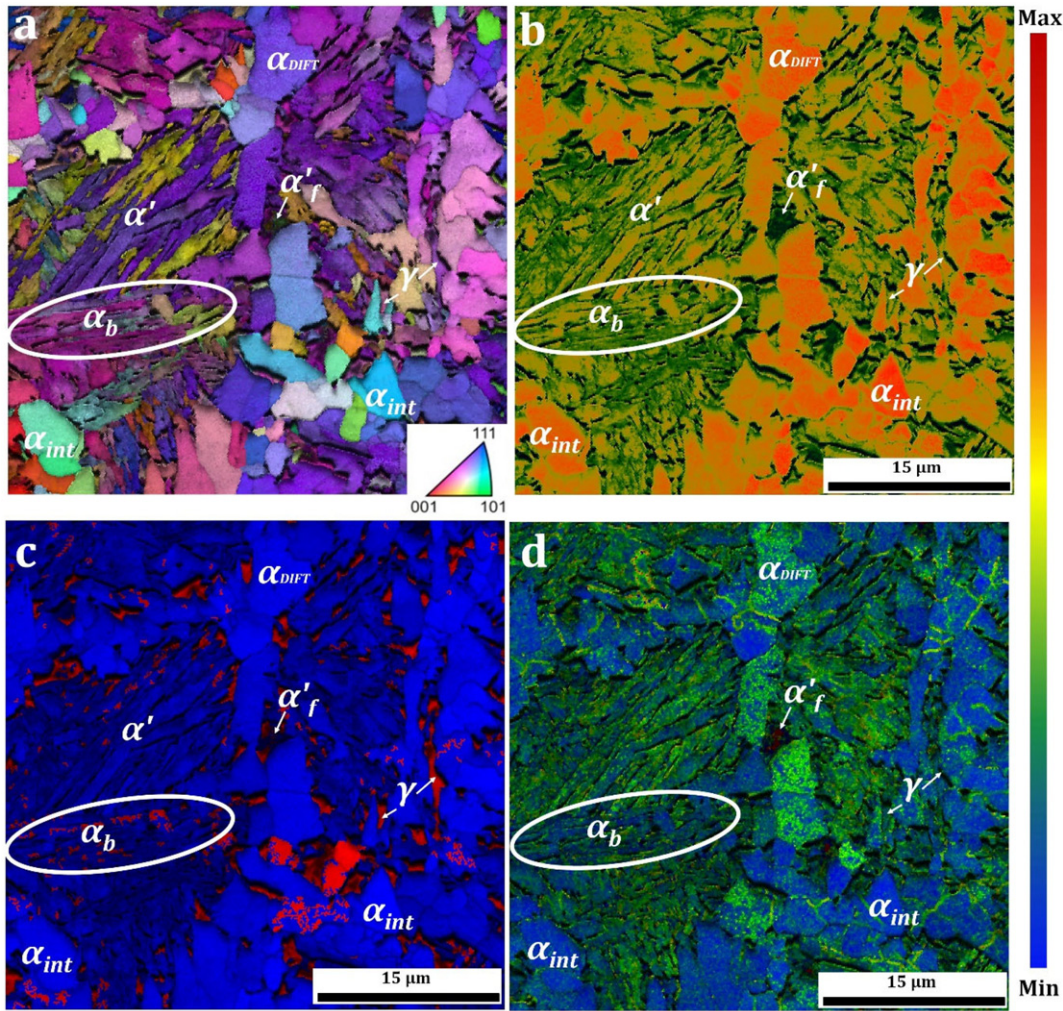


Fig. 3. Phase characterization of HSQ&P(328)₇₅₀ (a) Orientation Image Map (OIM), (b) confidence index, (c) phase map, and (d) KAM map.

ferrite grains. These carbon atoms can pile-up close to the interface forming a thin carbon-rich layer, which can constrain the growth of DIFT- α grains [12]. In other words, the carbon atoms diffuse from the DIFT and proeutectoid ferrite into untransformed austenite, leading to the development of ultrafine ferrite with very low carbon content. The morphology of this type of ferrite is very similar to epitaxial ferrite, which is formed by growth of the inter-critical ferrite (α_{int}). However, α_{int} grains contain a small dislocation amount and less distortion coming from neighboring crystals, when compared to the DIFT- α grains. Therefore, α_{int} and epitaxial ferrite have lower KAM values in comparison with DIFT- α grains, as indicated by light blue and green colors in Fig. 3c and d. The applied load during hot deformation accelerates the dynamic phase transition of austenite into DIFT- α [33,52], due to increased nucleation of the BCC phase on austenite crystalline defects. The diffusion of solute atoms, evolution of dislocation arrangements, and propagation of boundaries are factors that control these dynamic processes. Tong and Yang et al. [53,54] studied the formation of ultrafine grain and the effect of carbon distribution of DIFT- α in low carbon steels. They reported that DIFT should occur after dynamic recovery and/or recrystallization above Ar3 temperature, which is responsible for slight increasing the local deformation (or KAM). DIFT- α with remarkable low dislocation density and a slight deviation from the pattern of BCC Kikuchi bands is depicted by light green. Additionally, the inter-critical ferrites were developed along compact {101} planes with the lowest interatomic distance, leading to a decrease in local distortion due to dislocation annihilation by climb or cross-slip.

The local crystal distortion inside individual grains under plastic deformation can be characterized by Kernel analysis [55]. KAM quantifies the average misorientation around a measuring point with respect to a defined set of nearest neighbor points, considering the maximum value of 5° for crystal misorientation [56]. Thus, the KAM distribution expresses the local gradient of deformation and the distribution of localized plastic deformation in the grain scale. Therefore, this could be a great tool to identify deformation gradients due to phase transformation. Low Kernel values ($<0.5^\circ$) indicate low distortion of the specific crystal with respect to its neighbor. Fresh martensite produced after Q&P, from unstable retained austenite, showed the greatest lattice distortion (between 4 and 5°). In general, the KAM value distribution can characterize the phase distribution (i.e., DIFT- α , inter-critical ferrite, bainite, martensite, and fresh martensite) by analyzing the local deformations of microstructural features. The fraction of each microconstituent in the TRIP steels is essential to control the final mechanical behavior.

Generally, slip occurs in the {111} family of directions on compact {110} and {112} slip systems in BCC metals. Chin et al. [57] and Hutchinson [58] assumed that pencil glide occurs at any plane containing the {111} directions when the required critical BCC shear stress is satisfied. Consequently, the dislocation mobility in BCC metals does not obey Schmid's law due to non-glide stresses [59,60].

Taylor factor analysis was suggested to correct this discrepancy by treating each crystal's behavior based on its neighboring crystals. Taylor factor evaluates crystal deformation as a function of its specific critical

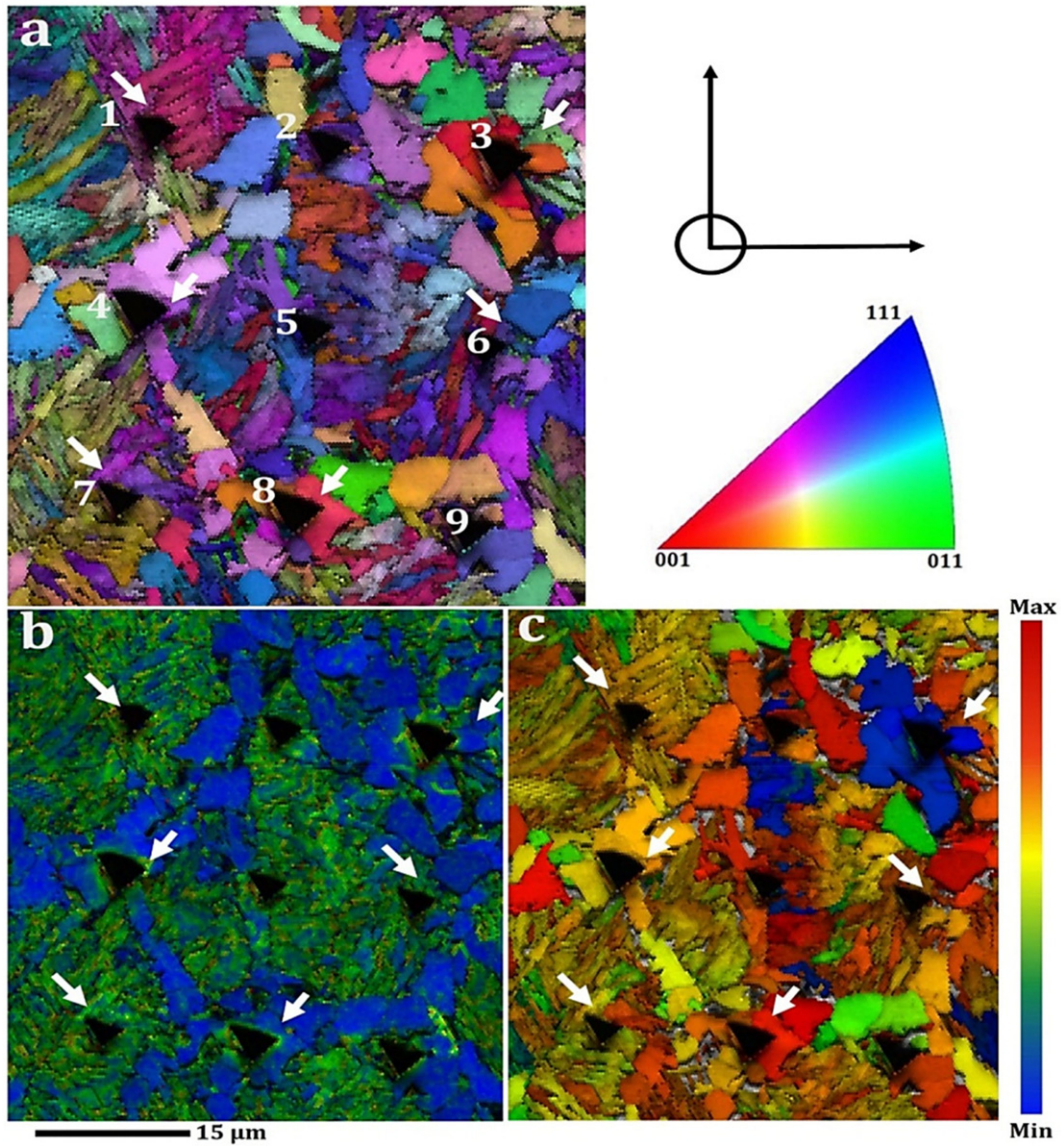


Fig. 4. Nanoindentation marks in the HSQ&P(328)₈₀₀ sample combined with: (a) Orientation Image Map (OIM); (b) Kernel Average Misorientation, and (c) Taylor factor map.

resolved shear stress (CRSS) of the activated slip system for a specific crystal orientation and the neighboring crystals. Three types of grains are classified using Taylor factor analysis. First are the low Taylor factor

grains with the lowest critical resolved shear stress (τ_{CRSS}), which are activated slip planes that are already aligned and deform in the first stages of plastic deformation. Second are the soft grains with moderate

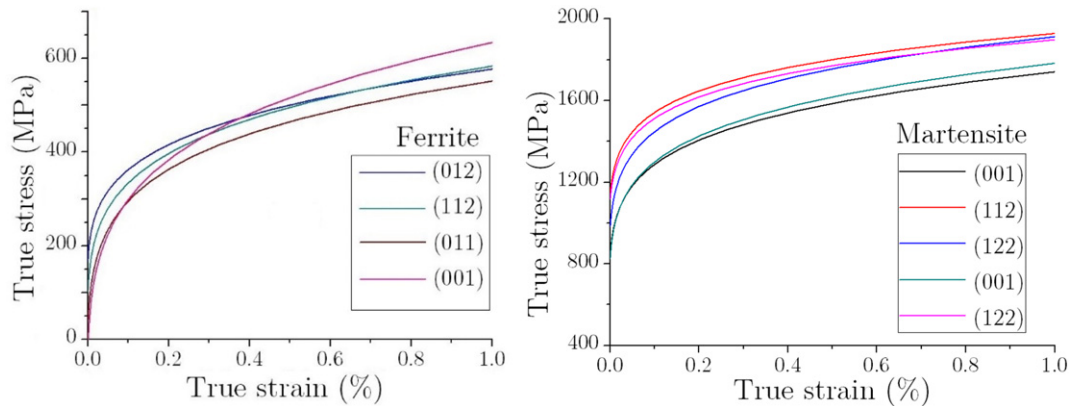


Fig. 5. Effect of grain orientation on tensile mechanical properties of ferrite (left) and martensite (right).

Taylor factor values, which are not oriented along activated slip systems. These grains rotate to new positions where they reach adequate τ_{CRSS} to start deformation. Thirdly, are hard grains with high Taylor factor (indicated in red in Fig. 4c) which are not aligned along the slip planes and cannot rotate easily to provide suitable active slip systems. These are brittle grains with high yield stress and they are prone to microcracks formation, which have been reported in various surveys [61–63].

3.2. Correlation between crystallographic orientation and localized mechanical properties

3.2.1. Image quality, Taylor factor, and KAM

In Fig. 4, the points numbered 3, 4, and 8 indicate ferrite grains with low, moderate, and high Taylor factor values, respectively. Their stress-strain curves were calculated using a reverse algorithm from the load-depth curves obtained by nanoindentation analyses [32]. The calculated yield stresses and hardening rates (n) were estimated as 386, 412, 469 MPa and 0.07, 0.19, and 0.28, respectively (Fig. 5). The values measured for higher hardening regions, i.e., $0.3 < n \leq 0.5$, in the Q&P and HSQ&P steels studied fall in the range for which a unique solution for mechanical properties can be obtained from the proposed reverse algorithm ($\sigma_y/E^* < 0.03$) [64]. The results show a direct correlation between Taylor factor, yield stress, and hardening rate in BCC grains. Grains with low Taylor value can be easily deformed under plastic deformation. Local crystal rotation provides suitable slip systems, operating with lower critical resolved shear stresses, enhancing the deformation of the microstructure. As a result, dislocation slip occurs more readily in $\langle 111 \rangle$ direction in tilt plane $\{110\}$ and $\{112\}$ in points 3 and 4, which correspond to the compact crystal planes in BCC. In the nanoindentation point 8, the non-close-packed $\{001\}$ planes with the largest interplanar spacing increases the strain hardening coefficient, due to the high driving force required for dislocation movement. Consequently, the region of nanoindentation 8 – with a high Taylor factor ferrite grain – shows excessive yield stress and hardening rates indicating grains with very fragile behavior [65–67].

3.2.2. Effect of grain orientation on tensile mechanical properties

The stress-strain curves for martensite grains were also calculated from the load-depth curve obtained by nanoindentation analyses and are presented in Fig. 5 and Table 1. Martensite has higher yield stress due to several factors such as a much higher dislocation density, strain needed to induce martensite transformation, lattice micro-strains, and stacking faults. It is worth mentioning that the mechanical and hardening behavior of fresh martensite with high dislocation density and carbon content are different from those of low carbon martensite, especially in the early stages of deformation [68]. Fresh martensite with high carbon content has higher tetragonality, which would hinder cross-slipping of the screw components of dislocations, which could lead to excessive yield stress and hardening rates. The Kernel values are similar in the points 1, 2, 5, 6, and 7 marked in Fig. 4(a) due to local misorientation variations related with the intrinsic lattice

microstrains. There is a clear relationship between the mechanical properties and grain orientation. It is worth mentioning that with the load applied large indentation depths were produced and the influence of size effects could be reduced. The martensite lath morphology oriented along non-compact $\{001\}$ planes, parallel to strain direction (SD), with cleavage planes parallel to laths interfaces provide brittle behavior (i.e., highest yield stress, ≈ 1610 MPa, and hardening rate, 0.49), as observed in nanoindentation point 1. Low toughness and brittle behavior of non-compact $\{001\}$ planes, parallel to SD, is attributed to the lowest surface energy and the largest interatomic spacing, which could result in a higher probability of microcrack initiation and cleavage propagation in this plane [69]. On the other hand, the nanoindentation point 7 shows moderate mechanical behavior (calculated yield stress and hardening rate were 1410 MPa and 0.34, respectively) as it is located on a low critical resolved shear stress martensite lath region, oriented with $\{112\}$ planes//SD.

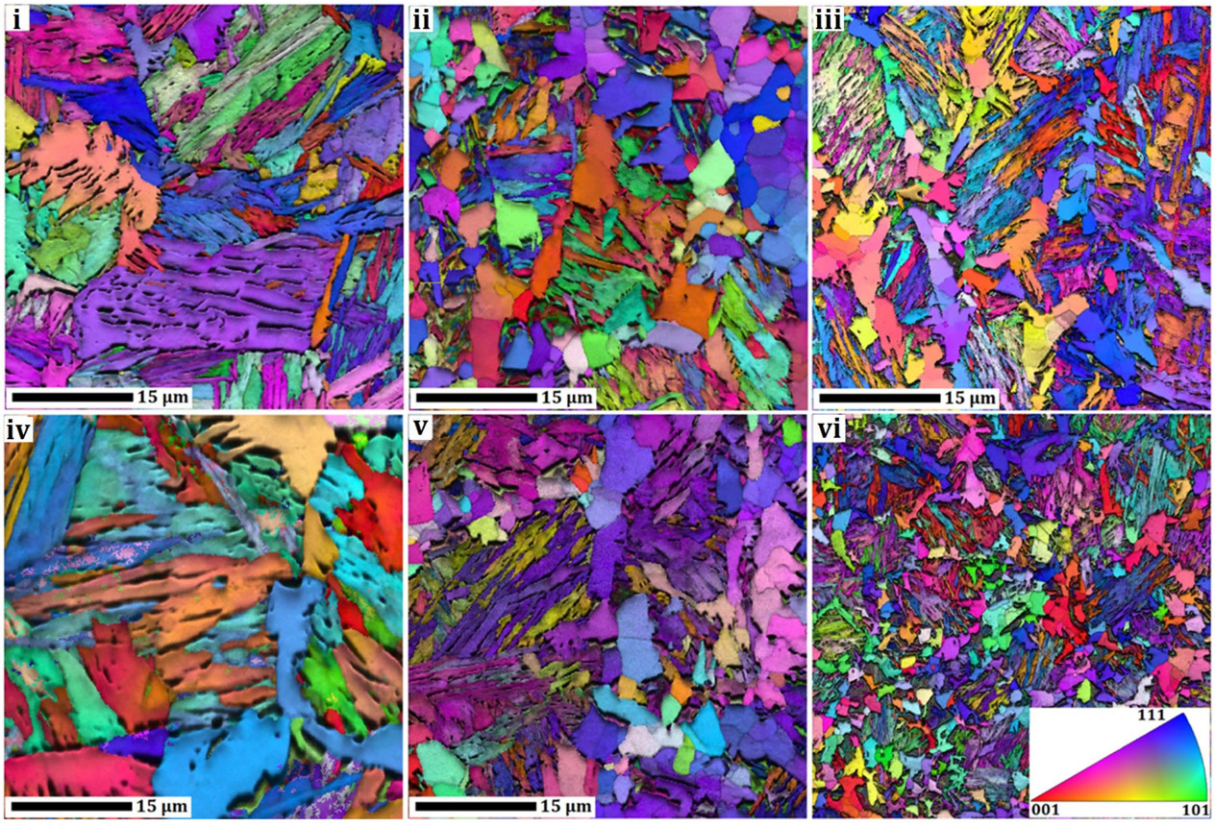
3.2.3. Effect of thermomechanical processing on OIM, KAM, and Taylor factor

Orientation image, KAM and, Taylor maps obtained from EBSD measurements of the six different studied conditions are shown in Fig. 6(a), (b), and (c), respectively. Comprehensive information obtained by EBSD is listed in Table 2. Multiphase microstructure and the volumetric fraction of each microconstituent play a significant role on macroscopic-scale mechanical properties. Face-centered cubic (FCC) Kikuchi pattern characterizes retained austenite in the samples, while body-centered cubic (BCC) Kikuchi patterns characterize a wide range of ferrites, such as epitaxial, inter-critical, bainitic-ferrite and DIFT, and martensite. For instance, DIFT-ferrite indicates moderate KAM values with high image quality pattern, inter-critical ferrite exhibits low KAM values with high IQ, and martensite presents moderate KAM and IQ values. Geometrically Necessary Dislocations (GND) are generated as excess dislocations within a Burgers circuit to satisfy geometrical compatibility between the grains and strain gradients due to geometrical constraints of the crystal lattice. GND also accommodate local incompatibilities of crystallographic parameters and are associated with heterogeneous deformation. In general, epitaxial and inter-critical ferrites control ductility, while strength is enhanced by bainitic-ferrite and martensite. Retained austenite (i.e., volume fraction and its orientation) enhances the work hardening rate and improves strength and ductility due to the shear transformation TRIP-effect, thereby delaying fracture.

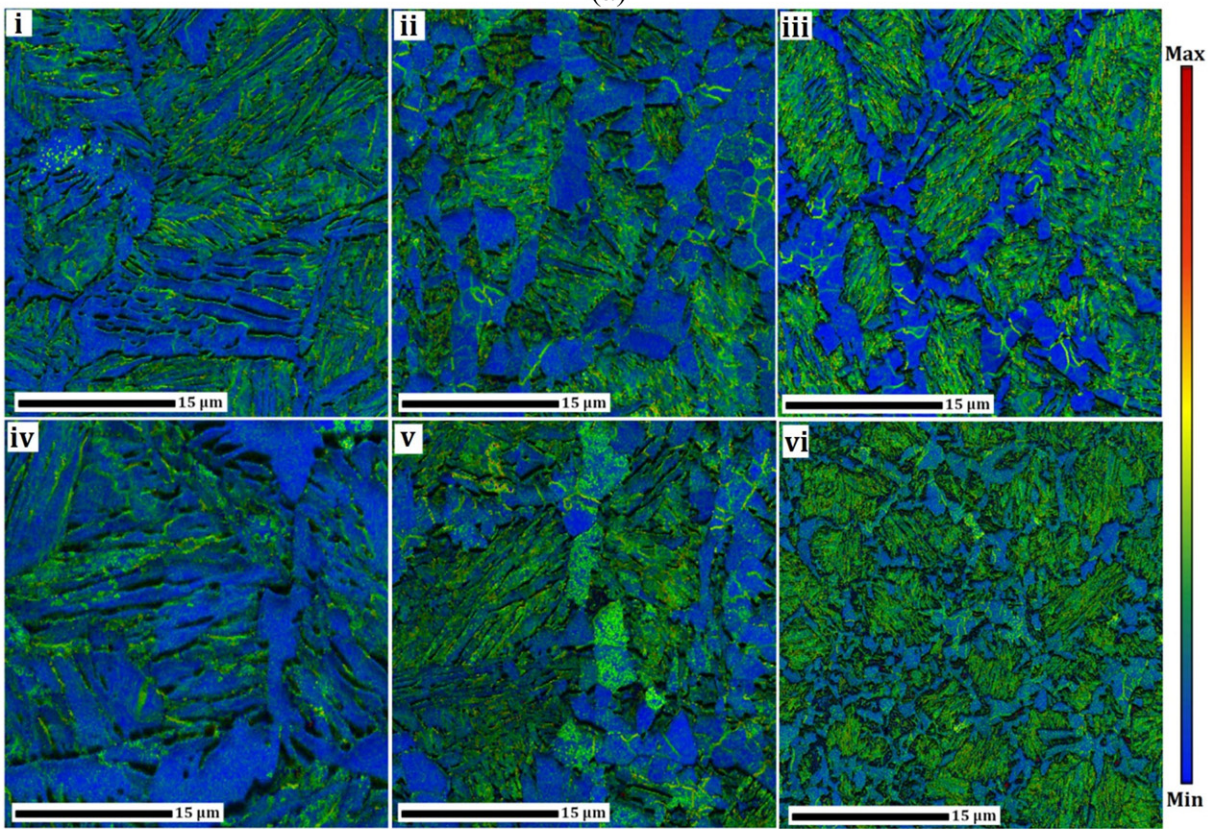
The results show that HSQ&P samples have a slightly greater volume fraction of retained austenite in comparison with Q&P process. This could be explained by the greater carbon content rejected to austenite by the ferrite growth during the deformation at the inter-critical temperature (DIFT-effect). Higher percentages of retained austenite are observed in the samples deformed at 750 °C. Thereby, HSQ&P(318)₇₅₀ and HSQ&P(328)₇₅₀ samples with the highest volume fraction of retained austenite show greater work hardening exponents and plasticity, due to the TRIP effect. It is notable that although HSQ&P(318)₇₅₀ sample exhibited the highest fraction of retained austenite ($\approx 4.8\%$) among other samples, the predominance of non-compact cleavage $\{100\}$ planes in both BCC and FCC phases, might deteriorate the mechanical properties. It should be stressed that the volume fraction of retained austenite measured by EBSD is lower than X-ray diffraction measurements (e.g., $\approx 4.8\%$ by EBSD and $\approx 10.4\%$ by XRD [24]) due to: the limits of the spatial resolution of the EBSD systems, as the smallest austenite laths cannot be resolved by EBSD but are detectable with X-ray diffraction; because of austenite transformation to martensite during mechanical preparation on the sample surface; and because of the penetration depth of X-rays is greater than that of electrons [24]. Consequently, EBSD measurements are known to provide underestimation in the determination of the volume fraction of retained austenite [46,70,71]. This is caused by several factors, such as strain-induced transformation, sampling size effects, and lack of penetration [72]. Thereby, XRD investigates the average behavior of an aggregate of grains and higher

Table 1
Calculated Euler angles and tilt angles for martensite and ferrite grains and their corresponding mechanical properties for the nanoindentations labeled in Fig. 4.

Point	Phi1	Phi	Phi2	Plane	Tilt angle (°)	Phase	ER	YS (MPa)	n
1	121.6	99.5	167.6	001	37.2	Martensite	226	1610	0.49
2	328.9	68.9	34.6	112	18.0	Martensite	191	326	0.02
3	317.7	175.9	217.7	011	42.9	Ferrite	220	386	0.07
4	346.1	149.5	236.5	112	25.2	Ferrite	198	412	0.19
5	245.4	64.3	318.5	122	37.8	Martensite	201	1570	0.47
6	259.0	65.3	304.2	001	57.4	Martensite	206	1430	0.36
7	150.5	89.8	155.8	122	49.9	Martensite	192	1410	0.34
8	228.2	83.1	355.7	001	38.4	Ferrite	227	469	0.28
9	199.0	136.8	52.8	012	43.2	Ferrite	180	453	0.29



(a)



(b)

Fig. 6. (a) OIM; (b) KAM and; (c) Taylor maps of diverse samples subjected to different Thermomechanical processing; (a) Q&P(318), (b) HSQ&P(318)₇₅₀, (c) HSQ&P(318)₈₀₀, (d) Q&P(328), (e) HSQ&P(328)₇₅₀, and (f) HSQ&P(328)₈₀₀.

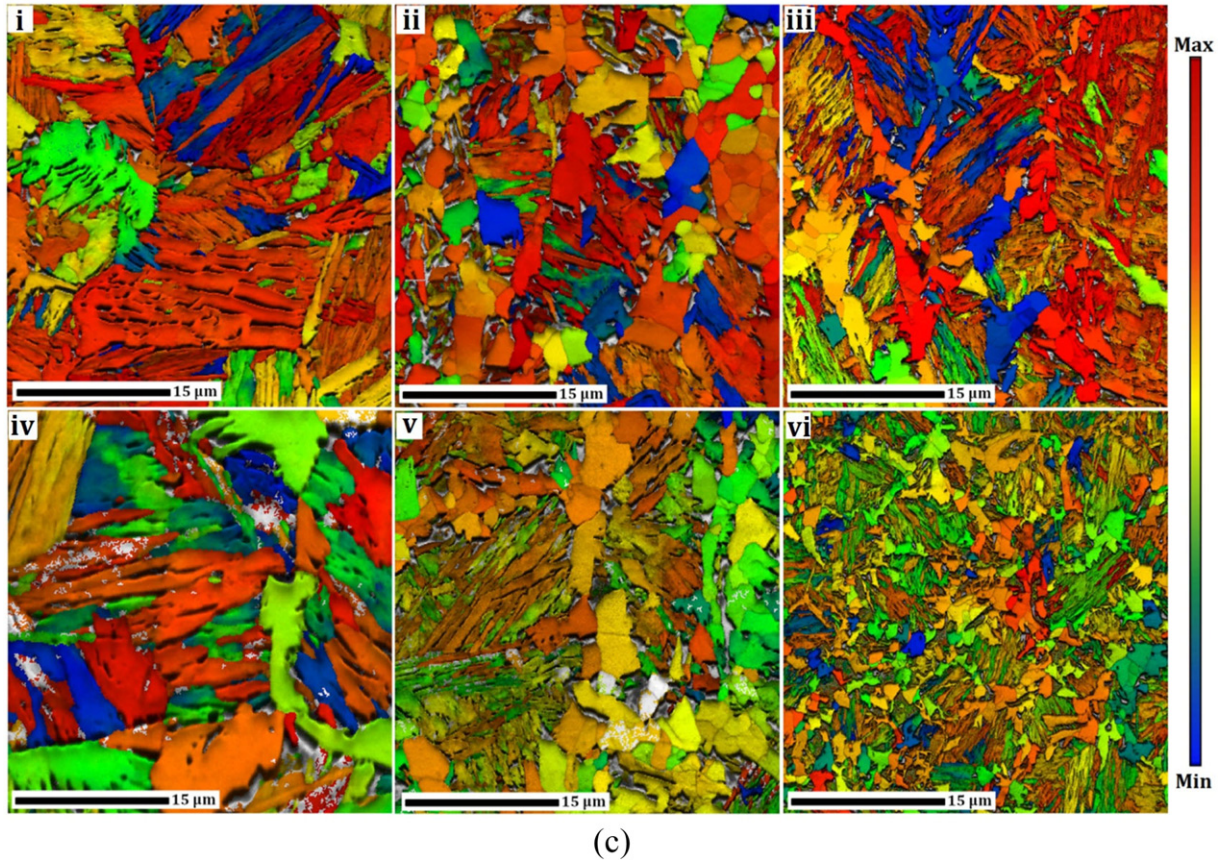


Fig. 6 (continued).

densities of dislocation and stacking fault, while, EBSD data provides detail information about specific crystallographic lattice orientation, local change of lattice orientation, and interphase boundaries in a micro-scale area [73]. Thus, EBSD information is more accurate at the surface; however, the volume fraction of phases obtained by XRD can be more reliable. In addition, several studies have shown that there is an evident reduction in austenite volume fraction as deformation amount increases. In Poling et al. [74] research with Q&P steels, it was displayed that the retained austenite fraction was decreased to 50% when a $\approx 10\%$ plastic deformation was applied, while Zou et al. [75] observed that with 5% plastic deformation almost all the retained austenite (25%) was transformed into martensite. Ding et al. [76] and Song et al. [77] showed that the volume fraction of retained austenite decreased to $<4\%$ and 2% , respectively, when the deformation reaches 20% . Zhao et al. [78] also showed that the volumetric fraction of austenite in steels treated by Q&P and Q&P-T (when tempering is applied to Q&P treated steels) is reduced from about 9% to $<4\%$ when the deformation reaches 13% . In the present investigation a 30% deformation was applied. Hence, the HSQ&P process describes an additional advantage, by which the component is already plastic deformed when the process ends and there is a reasonable fraction of retained austenite still available with considerable stability to benefit the TRIP effect. In addition, the volume fraction of ferrite progressively increases with the partitioning temperature due to the decreasing free energy barrier associated with γ/α transformation [79]. By increasing the partitioning temperature, the carbon partitioning from martensite is increased, leading to the formation of tempered martensite with less stored energy and hardness.

The average grain size of BCC phase was estimated as $1.37 \pm 0.10 \mu\text{m}$, $1.16 \pm 0.10 \mu\text{m}$, $0.88 \pm 0.10 \mu\text{m}$, $1.15 \pm 0.10 \mu\text{m}$, $1.03 \pm 0.10 \mu\text{m}$, and $0.77 \pm 0.10 \mu\text{m}$ for Q&P(318), HSQ&P(318)₇₅₀, HSQ&P(318)₈₀₀, Q&P(328), HSQ&P(328)₇₅₀, and HSQ&P(328)₈₀₀, respectively. Grain size reduction

was observed in hot stamping samples due to dynamic recrystallization of ferrite that accompanies the DIFT effect. Smaller grains lead to grain boundary strengthening according to the well-known Hall-Petch (HP) relationship (grain size–yield strength relationship) [80,81]. The grain refinement due to hot stamping can suppress the formation of fresh martensite by avoiding carbon clustering at intrinsic lattice defects in austenite. However, HSQ&P(318)₈₀₀ and HSQ&P(328)₇₅₀ samples with the highest fractions of fresh martensite are prone to microcracking and early fracture. Untransformed austenite can easily transform into bainitic-ferrite during the partitioning stage. This can be explained by the greater ferrite volume fraction in the HSQ&P samples when compared to Q&P samples.

Dislocation densities in polycrystalline materials are estimated by dislocation multiplication, dislocation movements, and their mutual interactions (i.e., recovery, grain boundaries, and second phase) [82,83]. Two phenomena have been proposed to evaluate dislocation densities using EBSD data: geometrically necessary dislocations (GNDs) and statistically stored dislocations (SSDs). GNDs estimate the dislocation accumulation within a Burger's circuit which contributes to lattice curvature. In contrast, no curvature of the crystal lattice at length scales larger than the Burger's circuit is considered in SSDs [84]. Jiang et al. [85] reported that dislocation density estimated by the effect of SSDs is lower than that estimated by the effect of GNDs. Therefore, dislocation density calculation in this research considered only GNDs effect.

3.3. Crystallographic textures and lattice distortions after Q&P and HSQ&P treatments

KAM and GND can estimate the amounts of crystallographic defects and lattice distortion from collected EBSD data. KAM is calculated from the average misorientation angle between a specific point and its

Table 2
Phase identification, Taylor factor, KAM, boundaries and BCC and FCC orientations related to the thermomechanical processing.

Sample	Phase identification (vol%)				Taylor factor			KAM			Boundaries			BCC orientation			FCC orientation		
	Retained austenite	Ferrite	Bainite/martensite	Fresh martensite	Low	Medium	High	Low	Medium	High	Low	High	CSL	{001}	{111}	{011}	{001}	{111}	{011}
Q&P(318)	1.68	34.30	61.82	2.20	17.76	21.93	60.30	45.66	38.35	16.00	55.60	36.65	7.66	14.04	32.00	8.77	7.81	18.75	30.00
HSQ&P(318) ₇₅₀	4.80	35.90	56.10	3.20	22.80	24.80	52.30	24.19	48.39	3.76	45.82	47.45	6.72	30.00	29.99	7.25	36.00	5.63	19.72
HSQ&P(318) ₈₀₀	2.80	43.30	52.50	1.40	30.20	27.20	42.50	16.62	33.25	1.20	40.90	23.90	5.20	20.97	35.00	6.45	6.06	16.67	27.27
Q&P(328)	1.02	22.00	75.68	1.30	6.37	27.30	66.30	58.85	28.66	12.50	54.76	41.63	3.61	39.00	13.33	13.33	18.75	7.81	21.88
HSQ&P(328) ₇₅₀	3.64	47.40	46.16	2.80	23.20	31.20	45.50	21.40	42.81	3.39	54.31	40.52	5.11	6.90	22.41	6.90	15.38	9.62	9.62
HSQ&P(328) ₈₀₀	2.34	59.60	32.46	5.60	24.60	42.90	32.30	17.11	34.23	2.58	30.24	31.79	7.97	28.00	20.63	7.94	10.20	10.20	31.00

nearest neighbors or pixels (i.e., fixed neighbor distance). This parameter is used to quantify the local strain build-up and qualify dislocation walls substructure. Azzeddine et al. [86] reported that GND dislocations in the cells/sub-grains walls are largely responsible for the evolution of the stored energy. The variation of KAM and GND of all investigated samples is presented in Fig. 7. A direct relation was observed between KAM and GND. The highest values of both were observed in the Q&P samples, which could be responsible for heterogeneous deformation and early fracture. Apparently, strain relief occurred in the HSQ&P samples. Zheng et al. [87] reported that the refined ferrite grains derived from the DIFT effect are responsible for the decrease of local distortion, reducing the KAM and GND levels. In addition, the homogeneous distribution of refined ferrite grains results in a simultaneous increase of strength and ductility. Therefore, it is expected that hot stamping improves the mechanical performance by reducing the stored internal energy due to dynamic recrystallization. The results showed that increasing the martensite volume fraction increased the overall GND density in the Q&P samples. Moreover, hot stamping process increased the number of refined recrystallized grains with low stored energy, resulting in lower fraction of martensite packets.

EBSD measurements also permit the qualitative evaluation of small local deformation gradients associated with orientation gradients inside each individual grain/phase – internal stresses due to the dislocation pile-ups containing dislocation walls or cell structures – and with the rotation of the crystalline lattice. It is well known that stress concentration, mechanical properties and stability of the grains depend on crystallographic orientation, which also controls the ability of dislocations to move along close-packed planes. Considering that the highest dislocation densities appear at the martensite/austenite or bainite/austenite interfaces due to lattice discontinuities [88], a local lattice stamping can activate sufficient slip systems due to dislocation pile-ups, which are essential to initiate displacive martensitic transformation. The crystallographic orientation distribution in BCC phase of all investigated samples was calculated from EBSD data. Normal direction inverse pole figure (IPF) maps are presented in Fig. 8. The grain orientation along {111}//SD with about 20° deviation was predominant in Q&P (318), while more intense {001}//SD texture was formed in Q&P (328). It is well documented that slip occurs easily along <111> crystallographic directions due to its highest atomic density. However, dislocations cannot move to the adjacent plane in <001> direction due to the large inter-atomic spacing, causing dislocation piles-up and generating localized strain concentration. Crystal distribution analysis revealed that hot stamping at 750 °C increased the number of cleavage {001}//SD planes in both HSQ&P(318)₇₅₀ and HSQ&P(328)₇₅₀ samples. Desirable {111}//SD and {112}//SD planes corresponding to main slip planes were developed in HSQ&P(318)₈₀₀ and HSQ&P(328)₈₀₀ (hot strained at 800 °C), contributing to plastic deformation. Therefore, it is expected that HSQ&P(318)₈₀₀ and HSQ&P(328)₈₀₀ samples exhibit great ductility without losing strength, which is the main aim of this study.

Both the amount of retained austenite and its crystallographic orientation controls the mechanical properties by the TRIP effect – mainly the uniform elongation and the fracture toughness. This effect enables the retained austenite undergo gradual transformation to martensite, leading to a continuous increase in the work-hardening rate during plastic deformation [45,89]. It is well-known that carbon and other alloying elements (such as Si and Mn), austenite grain size, austenite morphology and crystallographic orientation are effective to stabilize the austenite [90,91]. The volume fraction of retained austenite in each sample was also listed in Table 2. In Q&P samples, carbon atoms diffuse from supersaturated martensite into untransformed austenite during the partitioning stage. Thereby, increasing the stability of austenite, and it remained untransformed at room temperature. Hot stamping at inter-critical temperature reduces austenite grain size, increasing the number of austenite grain boundaries as preferred sites to ferrite nucleation and leading to the formation of fine ferrite grains. Formation of ferrite by DIFT effect accelerates the carbon diffusion into austenite, leading to

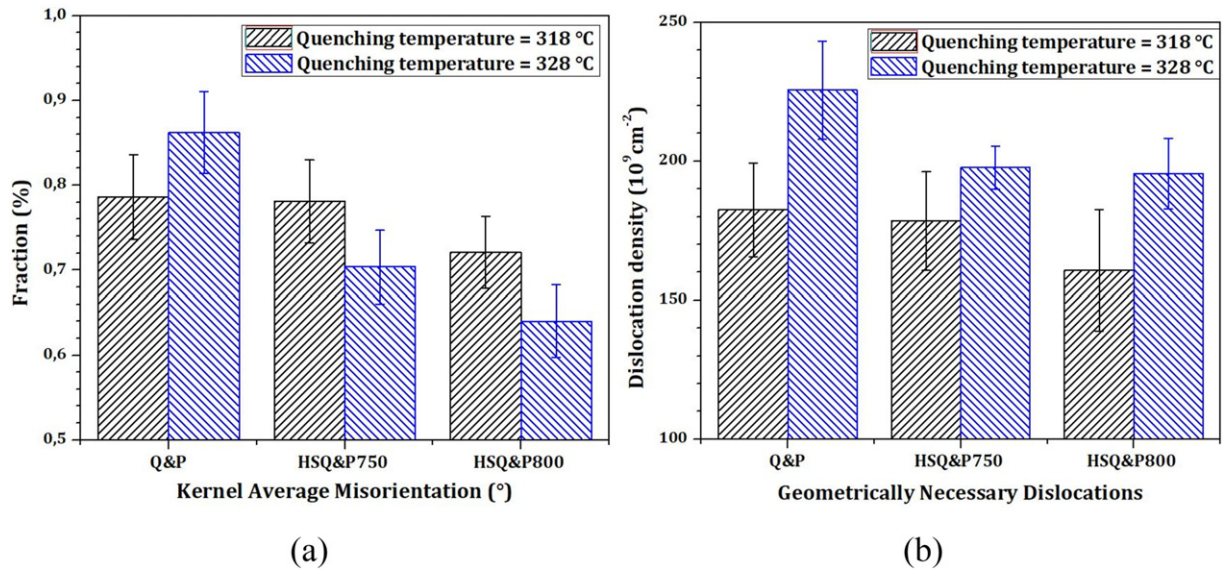


Fig. 7. Variation of local lattice distortion and dislocation densities using (a) KAM and (b) GND analyses from EBSD data.

an increase of the untransformed austenite stability. Therefore, a large amount of retained austenite was found in HSQ&P samples. The highest fraction of retained austenite occurs in samples subjected to hot stamping at 750 °C. Shen et al. [92] reported that the volume fraction, carbon content and the morphology of the untransformed austenite in low carbon content steel have a strong influence on its mechanical stability. Less stable retained austenite can be transformed in the early stage of deformation and thus reduce the effectiveness of TRIP effect. In addition, fine film-like retained austenite was identified in both samples hot strained at 800 °C. The fine film-like morphology is more stable than blocky retained austenite under deformation, even with lower

carbon content. Film-like retained austenite is generally surrounded by high strength constituents such as lath martensite and bainite. Thus, film-like retained austenite is under high hydrostatic pressure exerted by these phases, leading to greater restriction to volume expansion which is caused by the shear deformation associated with martensitic transformation [93,94]. Thus, by applying carbon-rich retained austenite films through Q&P process, both the resistance against hydrogen induced fracturing and toughness can be improved [95]. However, both thermal and mechanical stabilities must be ensured.

The orientation distribution function (ODF) is a mathematical function with an underlying statistical method using kernel density

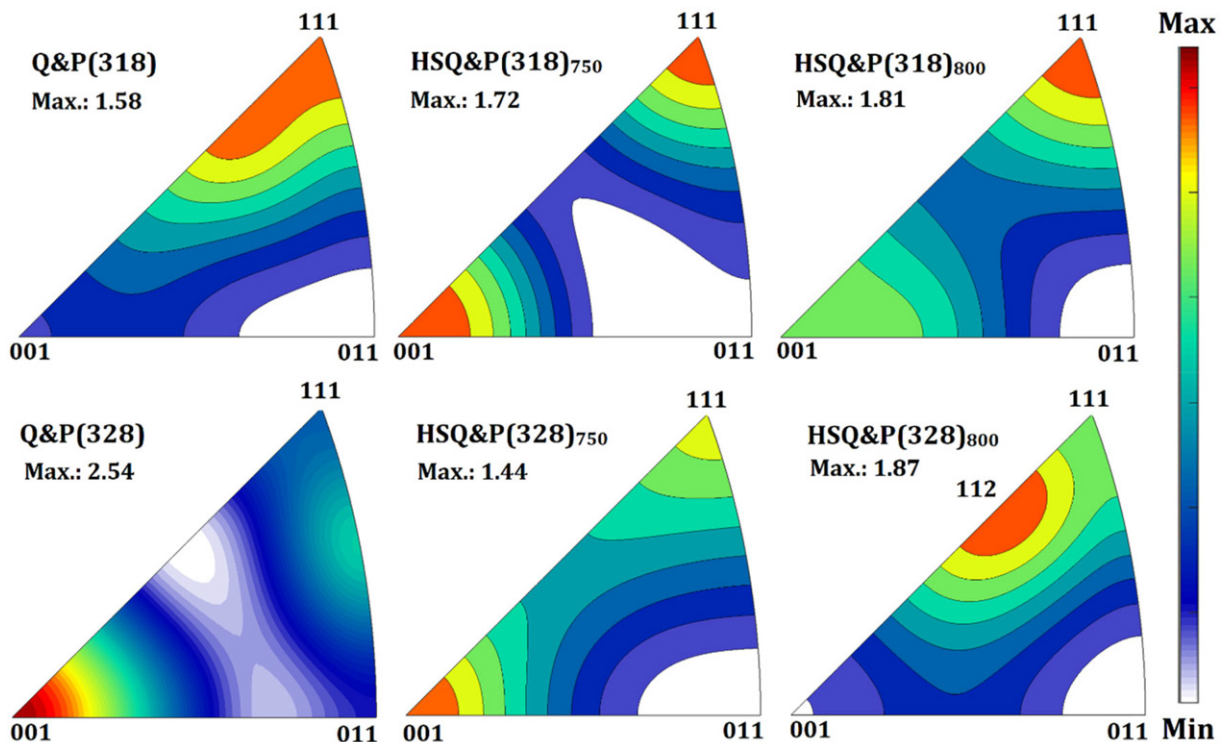


Fig. 8. IPFs of BCC phase: (a) Q&P(318), (b) HSQ&P(318)₇₅₀, (c) HSQ&P(318)₈₀₀, (d) Q&P(328), (e) HSQ&P(328)₇₅₀, and (f) HSQ&P(328)₈₀₀.

estimation, which describes the frequency of occurrence of particular crystal orientations in a three dimensional Euler space [96]. Grain orientation of the BCC and FCC in all investigated samples was calculated and presented by ODF at constant $\varphi_2 = 45^\circ$, on at least ten grains, based on kernel density estimation method, as shown in Fig. 9. The ODF results are in good agreement with previous IPF data. In BCC metals slip by dislocation motion, and is the main cause for plastic deformation, it is dependent on the transition temperature, for instance, in $\{112\}$, $\{110\}$, and $\{123\}$ planes the crystal slipping occurs at temperatures below of T_m (melting temperature)/4, between $T_m/4$ and $T_m/2$, and above $T_m/2$ (in Kelvin), respectively. The results indicate that the untransformed austenite were oriented along $\{110\}\langle 2\bar{2}1 \rangle$ and $\{223\}\langle \bar{1}10 \rangle$ in Q&P (318) sample, and $\{11\bar{1}\}\langle 101 \rangle$ in Q&P(328) sample. Retained austenite grains oriented along $\{001\}\langle 0\bar{1}0 \rangle$ were formed in HSQ&P(318)₇₅₀ sample. Ariza et al. [24] reported that $\{001\}$ //SD retained austenite cannot contribute well to plastic deformation by TRIP effect. The grains oriented along $\{001\}$ //SD which were dominant in HSQ&P(318)₇₅₀ and HSQ&P(318)₈₀₀ act as preferred sites to trans-granular quasi-cleavage fracture due to its low surface energy [97]. Thereby, no good mechanical behavior is expected for this sample. Compact plane and directions (i.e., $\langle 111 \rangle$ and $\langle 112 \rangle$ directions in $\{001\}$ planes dominant in the FCC structure) provides adequate slip system to facilitate dislocation movements and plastic deformation. Multiplication and interaction of dislocations during deformation enhance martensitic transformation and improve the tensile mechanical behavior. Finally, the intense $\{110\}$ //SD texture was observed in both HSQ&P(318)₈₀₀ and HSQ&P(328)₈₀₀ samples.

The distribution of dislocations is heterogeneous within the microstructure [87]. The vicinity of the grain boundaries (point-to-point misorientation $>15^\circ$) and triple junctions have high stored energy due to dislocation accumulation. However, local stored deformation energy

associated with crystalline distortion is identified within the individual grain (point-to-point misorientation $<15^\circ$). The distribution of boundaries in a deformed microstructure can be analyzed from the EBSD data. In general, dynamic recrystallization and recovery may occur during the hot deformation and partitioning stage, decreasing the crystallographic defects and stored energy. As reported by Parthiban et al. [12] the recrystallized prior austenite grains are responsible for the formation of a predominantly high angle grain boundaries martensite laths with small fractions of low angle boundaries. It should be noted that high amount of low angle boundaries in Q&P and HSQ&P₇₀₀ samples indicate grain subdivision mechanism. Hughes et al. [98] documented that the subdivision of grains occurred by dislocation piles up within the individual crystallites due to the lack of adequate slip systems associated with crystal orientation. This agrees with our previously mentioned KAM and GND dislocation results. Ferrite formation by DIFT-effect can cause local carbon enrichment or alloying elements segregation close to the grain boundaries. Thus, a necklace structure of new grains may be formed along the prior austenite grain boundaries. Ebrahimi et al. [99] reported that a necklace structure can be formed when high but different densities of dislocations pile up close to the grain boundaries of deformed or recrystallized grains. This prevents the growth and increases the number of high angle grain boundaries, which are preferred sites to ferrite nucleation. Thereby, resulting in low stored energy from the mentioned phenomena in the HSQ&P samples. In addition, it is notable that increasing the hot stamping temperature increases the grain boundary mobility and suppresses the recrystallization and nucleation of the α -phase.

From the results of microstructural features, it was predicted that samples hot strained at 800 °C followed by partitioning step could have optimum mechanical properties. The combination of ductile ferrite

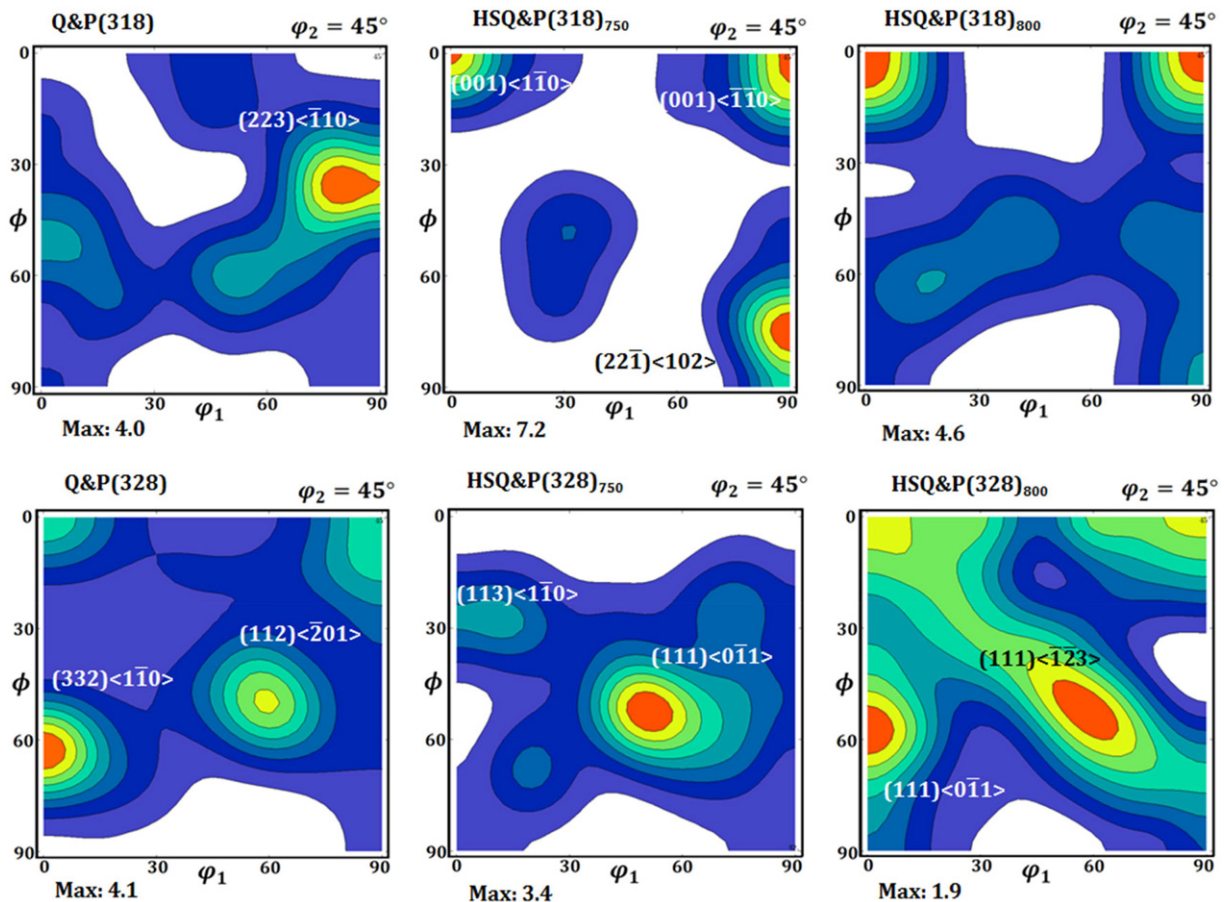


Fig. 9. ODF of FCC-retained austenite at constant $\varphi_2 = 45^\circ$; (a) Q&P(318), (b) HSQ&P(318)₇₅₀, (c) HSQ&P(318)₈₀₀, (d) Q&P(328), (e) HSQ&P(328)₇₅₀, and (f) HSQ&P(328)₈₀₀.

formed by DIFT effect - with low internal energy - and bainite/martensite in the microstructure can significantly improve the good ductility-high strength relation.

3.4. Tensile mechanical properties after Q&P and HSQ&P treatments

The stress-strain subsize curves and the mechanical properties of the samples are presented in Fig. 10 and listed in Table 3. Toughness was calculated by the total area below the stress-strain curve, which is a useful method to evaluate the ability of the material to absorb energy up to fracture. Santofimia et al. [100] reported that epitaxial ferrite formation introduced carbon content gradients in untransformed austenite, causing an enrichment close to the austenite grain boundaries. As a result, fragile fresh martensite with higher carbon content can be formed during the final quenching step, decreasing the mechanical properties and fracture toughness. Hence, deterioration of the mechanical properties and increase in brittle fracture are expected from the formation of fresh martensite [26]. The higher yield stress and the lower elongation were found in Q&P samples. These tensile mechanical properties can be explained by two distinct mechanisms: (i) high stored energy and high Taylor factor of BCC grains (bainite/martensite phase) with lack of enough slip systems to accumulate dislocation density and, (ii) formation of very brittle fresh martensite with supersaturated carbon content.

The HSQ&P samples with higher amount of retained austenite, due to DIFT effect, showed higher ductility and toughness when compared to the Q&P samples. Total elongation and absorbed energy results in HSQ&P samples are superior to those of Q&P obtained here and by other studies conducted on Q&P steels [70,101–104]. There are other researches on the development of the Q&P steels showing higher levels of total elongation and absorbed energy. Nevertheless, if Q&P steels are used for the manufacture of automotive structural components, they need to be stamped. As previously mentioned, this deformation process consumes part of the retained austenite and therefore its energy absorption capacity is reduced, in the case of a collision. In this way, the proposed HSQ&P process is favorable for manufacturing structural components, due to its final superior energy absorption capacity. A higher amount of retained austenite and suppression or reduction of the bainite formation during the partitioning stage improved the strength-ductility balance in the HSQ&P samples. Hot stamping at the intercritical temperature caused a reduction of austenite grain size, increasing the number of austenite grain boundaries as preferred sites to ferrite nucleation and promoting the formation of fine ferrite grains. Moreover, increasing the driving force by the stored deformation energy in deformed austenite grains increases the nucleation sites inside them and accelerates the carbon diffusion in austenite and the kinetics of the

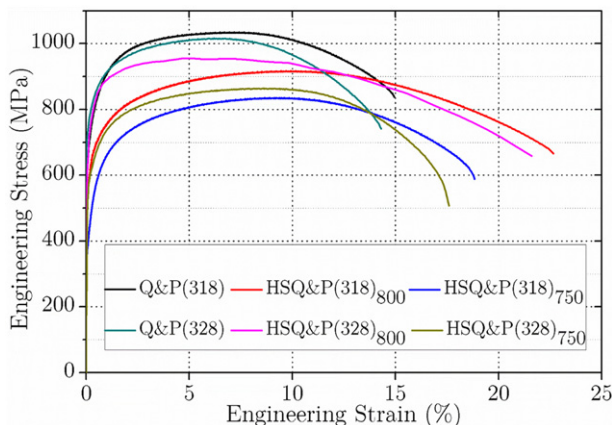


Fig. 10. Stress-strain curves at room temperature of all investigated specimens.

Table 3

Mechanical properties determined from tensile tests for the Q&P and HSQ&P samples.

Condition	ϵ_U (%)	ϵ_T (%)	σ_y (MPa)	UTS (MPa)	δ (GPa%)
Q&P(318)	8.9 ± 0.8	15 ± 0.8	978 ± 10	1035 ± 10	15,525 ± 1.0
HSQ&P(318) ₇₅₀	11.5 ± 0.7	19 ± 0.7	730 ± 15	835 ± 11	15,865 ± 1.2
HSQ&P(318) ₈₀₀	13.5 ± 0.6	23 ± 0.6	820 ± 17	920 ± 10	21,160 ± 1.5
Q&P(328)	8.1 ± 0.8	14 ± 0.8	963 ± 16	1016 ± 12	14,224 ± 1.1
HSQ&P(328) ₇₅₀	10.9 ± 0.9	17 ± 0.9	793 ± 15	835 ± 11	14,195 ± 1.0
HSQ&P(328) ₈₀₀	10.9 ± 0.9	22 ± 0.9	820 ± 20	955 ± 15	21,010 ± 1.5

ϵ_U , ϵ_T , σ_y , UTS, and δ are uniform elongation, total elongation, yield strength, ultimate tensile strength, and absorbed energy.

nucleation process of the ferritic phase. Thus, the localized intrinsic factors can increase the Gibbs free energy, lowering the austenite stability and accelerating the kinetics of the ferritic transformation [79]. The formation of newly ferrite by DIFT effect along prior austenite grain boundaries hinders the formation of fresh martensite and prevents early microcracks. It is postulated that DIFT- α at grain boundaries could reduce the stored energy and inhibit dislocation multi-slip within grains, as a result the rest austenite could be still be equiaxial. Although a high amount of blocky retained austenite was formed in HSQ&P₇₅₀, it may not be stable enough and cannot contribute significantly to improve the tensile mechanical properties. Fine film-like retained austenite under high hydrostatic pressure is more stable, enhancing the mechanical behavior of HSQ&P₈₀₀ samples. The favorable crystallographic orientation of these fine film-like retained austenite was along $\langle 111 \rangle$ and $\langle 112 \rangle // SD$, corresponding to the close-packed high dense atomic planes which facilitates adequate slip systems to enhance martensitic transformation. The great combination of strength and elongation obtained in HSQ&P₈₀₀ is obtained by the diverse microstructural features, such as grain size, distribution of precipitates on matrix microstructure, mechanisms of deformation, barriers in front of dislocation movements, slip deformation mechanisms, and crystallographic orientation. It is known that DIFT effect improves strengthening by grain refinement and work hardening behavior during deformation. On the one hand, DIFT mechanism destroys the initial band structure and causes a partial grain refinement, promoting the improvement of the mechanical properties without considerable loss of ductility. Recently, Lee et al. [105] demonstrated that carbon atoms diffused from ferrite generated by DIFT to the surrounding austenite, increasing its stability, and suppressing the formation of brittle martensite. On the other hand, dynamic recrystallization and dynamic recovery of ferrite can boost the mechanical properties. The increment of ferrite volume fraction reported in Table 2 can be explained by the occurrence of a DIFT-effect. According to this table, 9.3% and 37% of DIFT- α were produced in the samples HSQ&P(318) and HSQ&P(328), respectively. This increase is also directly associated with an increase of about 50% in total elongation observed in HSQ&P samples isothermally deformed. Hence, DIFT effect, dynamic recrystallization and recovery mechanisms could independently occur. Consequently, grain refinement could be controlled, firstly by dynamic recrystallization, and DIFT mechanism enhances newly fine ferritic grains by $\gamma \rightarrow \alpha$ DIFT transformation. The lower KAM values in HSQ&P(328&318)₈₀₀ in comparison with HSQ&P(328&318)₇₅₀ provides consistent conclusion related to the contribution of DIFT effect on the ductility.

4. Conclusions

A hot stamping and quenching and partitioning process has been proposed for optimizing the mechanical properties in TRIP-assisted steel. Electron backscattered diffraction and nanoindentation techniques were employed to characterize the microstructural features and their effect on mechanical performance. Estimated properties were verified by experimental sub-size tensile test. The utilized

techniques were able to characterize the microstructure and to predict the optimized mechanical behavior. From the obtained results, the following conclusions could be drawn:

- Excellent combination of mechanical strength and elongation can be obtained in samples subjected to hot stamping at 800 °C in 30% (true tensile strain), followed by quenching and partitioning (HSQ&P₈₀₀) at either the two quenching temperatures studied (318 and 328 °C).
- Desirable {111} and {112} grains parallel to the strain direction were developed in HSQ&P(318)₈₀₀ and HSQ&P(328)₈₀₀ samples. As the orientations are associated with principal slip planes, plastic deformation was enhanced.
- Predominance of {110}//SD texture in retained austenite grains and the presence of {111} and {112}//SD texture in BCC grains enhanced efficiently the TRIP effect.
- The distribution of localized plastic deformation in the grain scale as estimated by KAM values was successfully used to identify the DIFT-ferrite, inter-critical ferrite, bainite, martensite, and fresh martensite from the EBSD data.
- The resulting complex microstructure of the samples enhances the tensile strength due to work hardening caused by inter-critical ferrite and to the stability of the inter-lath film-like austenite, preventing the premature fracture by the martensitic transformation (TRIP-effect).
- The HSQ&P process describes an additional advantage, by which the component is already plastic deformed when the process ends and there is a reasonable fraction of retained austenite still available with considerable stability to benefit the TRIP effect.

Authorship contribution statement

The manuscript was written through contributions of all authors. All authors have given approval to the final version of the manuscript.

Declaration of competing interest

The authors declare that they have no known competing financial interests or personal relationships that could have appeared to influence the work reported in this paper.

Acknowledgments

The authors acknowledge the financial support given by São Paulo Research Foundation – FAPESP - Brazil (through Grants: 2014/11793-4 and 2019/24407-9), to Coordination for the Improvement of Higher Education Personnel – CAPES - Brazil (process number: 1715938), and to the Administrative Department of Science, Technology and Innovation – COLCIENCIAS – Colombia. To the Brazilian Nanotechnology National Laboratory (LNNano) for the use of the Gleeble®3800 thermomechanical simulator, and to Research Group Materiales de Ingeniería (GIMI) – Facultad de Tecnología Mecánica, Universidad Tecnológica de Pereira (UTP).

References

- [1] M. El Mehtedi, S. Spinarelli, J. Zrník, Effect of thermomechanical processing on the microstructure of Si-Mn TRIP steel, *La Metall. Ital.* 14 (2010) 56–60, [https://doi.org/10.1016/S1006-706X\(07\)60028-4](https://doi.org/10.1016/S1006-706X(07)60028-4).
- [2] S.M.K. Hosseini, A. Zarei-Hanzaki, S. Yue, Effects of ferrite phase characteristics on microstructure and mechanical properties of thermomechanically-processed low-silicon content TRIP-assisted steels, *Mater. Sci. Eng. A* 626 (2015) 229–236, <https://doi.org/10.1016/j.msea.2014.12.063>.
- [3] F. Huang, J. Yang, Z. Guo, Y. Rong, N. Chen, Dynamic compression property of a low-carbon quenching and partitioning steel, *Mater. Sci. Eng. A* 651 (2016) 224–232, <https://doi.org/10.1016/j.msea.2015.10.115>.
- [4] Z. Cai, H. Ding, R.D.K. Misra, H. Kong, H. Wu, Unique impact of ferrite in influencing austenite stability and deformation behavior in a hot-rolled Fe-Mn-Al-C steel, *Mater. Sci. Eng. A* 595 (2014) 86–91, <https://doi.org/10.1016/j.msea.2013.12.003>.
- [5] J. Speer, D.K. Matlock, B.C. De Cooman, J.G. Schroth, Carbon partitioning into austenite after martensite transformation, *Acta Mater.* 51 (2003) 2611–2622, [https://doi.org/10.1016/S1359-6454\(03\)00059-4](https://doi.org/10.1016/S1359-6454(03)00059-4).
- [6] G. Liu, S. Zhang, J. Li, J. Wang, Q. Meng, Fast-heating for intercritical annealing of cold-rolled quenching and partitioning steel, *Mater. Sci. Eng. A* 669 (2016) 387–395, <https://doi.org/10.1016/j.msea.2016.05.106>.
- [7] Y.J. Li, J. Kang, W.N. Zhang, D. Liu, X.H. Wang, G. Yuan, R.D.K. Misra, G.D. Wang, A novel phase transition behavior during dynamic partitioning and analysis of retained austenite in quenched and partitioned steels, *Mater. Sci. Eng. A* 710 (2018) 181–191, <https://doi.org/10.1016/j.msea.2017.10.104>.
- [8] J. Zhu, R. Ding, J. He, Z. Yang, C. Zhang, H. Chen, A cyclic austenite reversion treatment for stabilizing austenite in the medium manganese steels, *Scr. Mater.* 136 (2017) 6–10, <https://doi.org/10.1016/j.scriptamat.2017.03.038>.
- [9] M.C. Somani, D.A. Porter, L.P. Karjalainen, D.K. Misra, Designing a novel DQ&P process through physical simulation studies, *Mater. Sci. Forum* 762 (2013) 83–88, <https://doi.org/10.4028/www.scientific.net/MSF.762.83>.
- [10] X. Tan, Y. Xu, X. Yang, Z. Liu, D. Wu, Effect of partitioning procedure on microstructure and mechanical properties of a hot-rolled directly quenched and partitioned steel, *Mater. Sci. Eng. A* 594 (2014) 149–160, <https://doi.org/10.1016/j.msea.2013.11.064>.
- [11] X.-D. Tan, Y.-B. Xu, D. Pongé, X.-L. Yang, Z.-P. Hu, F. Peng, X.-W. Ju, D. Wu, D. Raabe, Effect of intercritical deformation on microstructure and mechanical properties of a low-silicon aluminum-added hot-rolled directly quenched and partitioned steel, *Mater. Sci. Eng. A* 656 (2016) 200–215, <https://doi.org/10.1016/j.msea.2016.01.040>.
- [12] R. Parthiban, S. Ghosh Chowdhury, K.C. Harikumar, S. Sankaran, Evolution of microstructure and its influence on tensile properties in thermo-mechanically controlled processed (TMCP) quench and partition (Q&P) steel, *Mater. Sci. Eng. A* 705 (2017) 376–384, <https://doi.org/10.1016/j.msea.2017.08.095>.
- [13] H. Liu, X. Lu, X. Jin, H. Dong, J. Shi, Enhanced mechanical properties of a hot stamped advanced high-strength steel treated by quenching and partitioning process, *Scr. Mater.* 64 (2011) 749–752, <https://doi.org/10.1016/j.scriptamat.2010.12.037>.
- [14] M. Karam-Abian, A. Zarei-Hanzaki, H.R. Abedi, S. Heshmati-Manesh, Micro and macro-mechanical behavior of a transformation-induced plasticity steel developed by thermomechanical processing followed by quenching and partitioning, *Mater. Sci. Eng. A* 651 (2016) 233–240, <https://doi.org/10.1016/j.msea.2015.10.116>.
- [15] M. Chen, R. Wu, H. Liu, L. Wang, J. Shi, H. Dong, X. Jin, An ultrahigh strength steel produced through deformation-induced ferrite transformation and Q&P process, *Sci. China Technol. Sci.* 55 (2012) 1827–1832, <https://doi.org/10.1007/s11431-012-4880-z>.
- [16] H. Liu, H. Sun, B. Liu, D. Li, F. Sun, X. Jin, An ultrahigh strength steel with ultrafine-grained microstructure produced through intercritical deformation and partitioning process, *Mater. Des.* 83 (2015) 760–767, <https://doi.org/10.1016/j.matdes.2015.06.047>.
- [17] X. Han, Y. Zhong, K. Yang, Z. Cui, J. Chen, Application of hot stamping process by integrating quenching & partitioning heat treatment to improve mechanical properties, *Procedia Eng* 81 (2014) 1737–1743, <https://doi.org/10.1016/j.proeng.2014.10.223>.
- [18] X. Han, Y. Zhong, P. Xin, Z. Cui, J. Chen, Research on one-step quenching and partitioning treatment and its application in hot stamping process, *J. Eng. Manuf.* (2015) 1–11, <https://doi.org/10.1177/0954405415616062>.
- [19] Y. Chang, G. Li, C. Wang, X. Li, H. Dong, Effect of quenching and partitioning with hot stamping on martensite transformation and mechanical properties of AHSS, *J. Mater. Eng. Perform.* 24 (2015) 3194–3200, <https://doi.org/10.1007/s11665-015-1579-x>.
- [20] X. Han, Y. Li, S. Chen, S. Tan, Y. Ding, J. Chen, Research on Q&P hot stamping process integrated with fractional cooling strategy, *Procedia Eng* 207 (2017) 705–710, <https://doi.org/10.1016/j.proeng.2017.10.1045>.
- [21] B.M. Linke, T. Gerber, A. Hatscher, I. Salvatori, I. Aranguren, M. Arribas, Impact of Si on microstructure and mechanical properties of 22MnB5 hot stamping steel treated by quenching & partitioning (Q&P), *Metall. Mater. Trans. A Phys. Metall. Mater. Sci.* 49A (2018) 54–65, <https://doi.org/10.1007/s11661-017-4400-7>.
- [22] Z. Wang, K. Wang, Y. Liu, B. Zhu, Y. Zhang, S. Li, Multi-scale simulation for hot stamping quenching & partitioning process of high-strength steel, *J. Mater. Process. Technol.* 269 (2019) 150–162, <https://doi.org/10.1016/j.jmatprotec.2019.02.008>.
- [23] M. Krugla, R. Rana, S. Das, Ductile ultra high strength hot stamped steel obtained by Q&P treatments, *Mater. Sci. Technol. (United Kingdom)*. 34 (2018) 268–281, <https://doi.org/10.1080/02670836.2017.1371409>.
- [24] E.A. Ariza, M. Masoumi, A.P. Tschiptschin, Improvement of tensile mechanical properties in a TRIP-assisted steel by controlling of crystallographic orientation via HSQ&P processes, *Mater. Sci. Eng. A* 713 (2018) 223–233, <https://doi.org/10.1016/j.msea.2017.12.046>.
- [25] E.A. Ariza, J. Poplawsky, W.E.I. Guo, P. Tschiptschin, K. Unocic, A.J. Ramirez, Evaluation of carbon partitioning in new generation of quench and partitioning (Q&P) steels, *Metall. Mater. Trans. A* 49 (2018) 4809–4823.
- [26] D. De Knijf, R. Petrov, C. Föjér, L.A.I. Kestens, Effect of fresh martensite on the stability of retained austenite in quenching and partitioning steel, *Mater. Sci. Eng. A* 615 (2014) 107–115, <https://doi.org/10.1016/j.msea.2014.07.054>.
- [27] G. Miyamoto, J.C. Oh, K. Hono, T. Furuhara, T. Maki, Effect of partitioning of Mn and Si on the growth kinetics of cementite in tempered Fe-0.6 mass% C martensite, *Acta Mater.* 55 (2007) 5027–5038, <https://doi.org/10.1016/j.actamat.2007.05.023>.
- [28] D.T. Pierce, D.R. Coughlin, D.L. Williamson, J. Kähkönen, A.J. Clarke, K.D. Clarke, J.G. Speer, E. De Moor, Quantitative investigation into the influence of temperature on

- carbide and austenite evolution during partitioning of a quenched and partitioned steel, *Scr. Mater.* 121 (2016) 5–9, <https://doi.org/10.1016/j.scriptamat.2016.04.027>.
- [29] F. HajjAkbar, J. Sietsma, G. Miyamoto, T. Furuhara, M.J. Santofimia, Interaction of carbon partitioning, carbide precipitation and bainite formation during the Q&P process in a low C steel, *Acta Mater.* 104 (2016) 72–83, <https://doi.org/10.1016/j.actamat.2015.11.032>.
- [30] Y. Toji, G. Miyamoto, D. Raabe, Carbon partitioning during quenching and partitioning heat treatment accompanied by carbide precipitation, *Acta Mater.* 86 (2015) 137–147, <https://doi.org/10.1016/j.actamat.2014.11.049>.
- [31] B. Zhu, J. Zhu, Y. Wang, B. Rolfe, Z. Wang, Y. Zhang, Combined hot stamping and Q&P processing with a hot air partitioning device, *J. Mater. Process. Technol.* 262 (2018) 392–402, <https://doi.org/10.1016/j.jmatprotec.2018.07.011>.
- [32] E.A. Ariza, A.S. Nishikawa, H. Goldenstein, A.P. Tschiptschin, Characterization and methodology for calculating the mechanical properties of a TRIP-steel submitted to hot stamping and quenching and partitioning (Q&P), *Mater. Sci. Eng. A* 671 (2016) 54–69, <https://doi.org/10.1016/j.msea.2016.06.038>.
- [33] H. Dong, X. Sun, Deformation induced ferrite transformation in low carbon steels, *Curr. Opin. Solid State Mater. Sci.* 9 (2005) 269–276, <https://doi.org/10.1016/j.cossms.2006.02.014>.
- [34] A. Fischer-Cripps, *Nanoindentation*, Springer, New York, 2011 <https://doi.org/10.1016/B978-0-12-387667-6.00013-0>.
- [35] E. Tam, *Characterization and Modification of the Mechanical and Surface Properties at the Nanoscale*, Université Libre de Bruxelles, 2010.
- [36] K.K. Tho, S. Swaddiwudhipong, Z.S. Liu, K. Zeng, Simulation of instrumented indentation and material characterization, *Mater. Sci. Eng. A* 390 (2005) 202–209, <https://doi.org/10.1016/j.msea.2004.08.037>.
- [37] S.A.R. Pulecio, M.C.M. Farias, R.M. Souza, Finite element and dimensional analysis algorithm for the prediction of mechanical properties of bulk materials and thin films, *Surf. Coatings Technol.* 205 (2010) 1386–1392, <https://doi.org/10.1016/j.surfcoat.2010.07.039>.
- [38] Z.S. Ma, Y.C. Zhou, S.G. Long, X.L. Zhong, C. Lu, Characterization of stress-strain relationships of elastoplastic materials: an improved method with conical and pyramidal indenters, *Mech. Mater.* 54 (2012) 113–123, <https://doi.org/10.1016/j.mechmat.2012.07.006>.
- [39] M. Dao, N. Chollacoop, K.J. Van Vliet, T.A. Venkatesh, S. Suresh, Computational modeling of the forward and reverse problems in instrumented sharp indentation, *Acta Mater.* 49 (2001) 3899–3918, [https://doi.org/10.1016/S1359-6454\(01\)00295-6](https://doi.org/10.1016/S1359-6454(01)00295-6).
- [40] R. Rodríguez, I. Gutierrez, Correlation between nanoindentation and tensile properties influence of the indentation size effect, *Mater. Sci. Eng. A* 361 (2003) 377–384, [https://doi.org/10.1016/S0921-5093\(03\)00563-X](https://doi.org/10.1016/S0921-5093(03)00563-X).
- [41] T.K. Eller, L. Greve, M. Andres, M. Medricky, V.T. Meinders, A.H. van den Boogaard, Determination of strain hardening parameters of tailor hardened boron steel up to high strains using inverse FEM optimization and strain field matching, *J. Mater. Process. Technol.* 228 (2016) 43–58.
- [42] J. Wu, P. Wray, C. Garcia, M. Hua, A. Deardo, Image quality analysis: a new method of characterizing microstructures, *ISIJ Int.* 45 (2005) 254–262, <https://doi.org/10.2355/isijinternational.45.254>.
- [43] K. Radwanski, Structural characterization of low-carbon multiphase steels merging advanced research methods with light optical microscopy, *Arch. Civ. Mech. Eng.* 16 (2016) 282–293, <https://doi.org/10.1016/j.acme.2015.12.001>.
- [44] L. Yuan, *Nanoscale Austenite Reversion Through Partitioning, Segregation and Kinetic Freezing in Martensitic Stainless Steels*, Max-Planck-Institute für Eisenforschung, 2012.
- [45] R. Petrov, L. Kestens, A. Wasilkowska, Y. Houbaert, Microstructure and texture of a lightly deformed TRIP-assisted steel characterized by means of the EBSD technique, *Mater. Sci. Eng. A* 447 (2007) 285–297, <https://doi.org/10.1016/j.msea.2006.10.023>.
- [46] G. Thomas, J. Speer, D. Matlock, J. Michael, Application of electron backscatter diffraction techniques to quenched and partitioned steels, *Microsc. Microanal.* 17 (2011) 368–373, <https://doi.org/10.1017/S1431927610094432>.
- [47] T.M. Rampton, S.I. Wright, M.P. Miles, E.R. Homer, R.H. Wagoner, D.T. Fullwood, Improved twin detection via tracking of individual Kikuchi band intensity of EBSD patterns, *Ultramicroscopy* 185 (2018) 5–14, <https://doi.org/10.1016/j.ultramic.2017.11.003>.
- [48] S.I. Wright, M.M. Nowell, R. De Kloof, P. Camus, T. Rampton, Electron imaging with an EBSD detector, *Ultramicroscopy* 148 (2015) 132–145, <https://doi.org/10.1016/j.ultramic.2014.10.002>.
- [49] M. Zhang, F. Zhu, Z. Duan, S. Ma, Characteristics of retained austenite in TRIP steels with bainitic ferrite matrix, *J. Wuhan Univ. Technol. Sci. Ed.* 26 (2011) 1148–1151, <https://doi.org/10.1007/s11595-011-0379-x>.
- [50] W. Wang, L. Zhang, M. Guo, L. Huang, X. Wei, Non-isothermal deformation behavior and FE simulation of ultrahigh strength BR1500HS steel in hot stamping process, *Int. J. Adv. Manuf. Technol.* (2016) <https://doi.org/10.1007/s00170-016-8656-7>.
- [51] J. Sietsma, Nucleation and growth during the austenite-to-ferrite phase transformation in steels after plastic deformation, in: E. Pereloma, D. Edmonds (Eds.), *Phase Transform. Steels*, Woodhead Publishing in Materials, Philadelphia 2012, pp. 505–554.
- [52] J. Choi, D. Seo, J. Lee, K. Um, W. Choo, Formation of ultrafine ferrite by strain-induced dynamic transformation in plain low carbon steel, *ISIJ Int.* 43 (2003) 746–754.
- [53] M. Tong, J. Ni, Y. Zhang, D. Li, Y. Li, Temporal oscillatory behavior in deformation induced ferrite transformation in an Fe-C binary system, *Scr. Mater.* 50 (2004) 909–913, <https://doi.org/10.1016/j.scriptamat.2003.11.033>.
- [54] Z. Yang, R. Wang, Formation of ultra-fine grain structure of plain low carbon steel through deformation induced ferrite transformation, *ISIJ Int.* 43 (2008) 761–766, <https://doi.org/10.2355/isijinternational.43.761>.
- [55] K. Hidaka, Y. Takemoto, T. Senuma, Microstructural evolution of carbon steels in hot stamping processes, *ISIJ Int.* 52 (2012) 688–696, <https://doi.org/10.2355/isijinternational.52.688>.
- [56] A.J. Schwartz, M. Kumar, B.L. Adams, D.P. Field, *Electron Backscatter Diffraction in Materials Science*, 2nd, illustr ed. Springer Science & Business Media, 2010.
- [57] G.Y. Chin, W. Mammel, M.T. Dolan, Taylor's theory of texture for axisymmetric flow in body-centered cubic metals, *Trans. Metall. Soc. AIME* 239 (1967) 1854–1855.
- [58] J.W. Hutchinson, Singular behaviour at the end of a tensile crack in a hardening material, *J. Mech. Phys. Solids*. 16 (1968) 13–31.
- [59] G.I. Taylor, C.F. Elam, The distortion of iron crystals, *Proc. R. Soc. A Math. Phys. Eng. Sci.* 112 (1926) 337–361, <https://doi.org/10.1098/rspa.1926.0116>.
- [60] G.I. Taylor, Mathematical and physical sciences the deformation of crystals of β -brass, *Proc. R. Soc. A Math. Phys. Eng. Sci. IV* (1927) 167–188.
- [61] X. Ran, D. Liu, J. Li, H. ming Wang, X. Cheng, J. kui Zhang, H. bo Tang, X. Liu, Effects of microstructures on the fatigue crack growth behavior of laser additive manufactured ultrahigh-strength AerMet100 steel, *Mater. Sci. Eng. A* 721 (2018) 251–262, <https://doi.org/10.1016/j.msea.2018.02.088>.
- [62] Z. Wang, S. Sun, B. Wang, Z. Shi, W. Fu, Importance and role of grain size in free surface cracking prediction of heavy forgings, *Mater. Sci. Eng. A* 625 (2015) 321–330, <https://doi.org/10.1016/j.msea.2014.12.022>.
- [63] S. Zhang, E. Fan, J. Wan, J. Liu, Y. Huang, X. Li, Effect of Nb on the hydrogen-induced cracking of high-strength low-alloy steel, *Corros. Sci.* 139 (2018) 83–96, <https://doi.org/10.1016/j.corsci.2018.04.041>.
- [64] N. Chollacoop, M. Dao, S. Suresh, Depth-sensing instrumented indentation with dual sharp indenters, *Acta Mater.* 51 (2003) 3713–3729, [https://doi.org/10.1016/S1359-6454\(03\)00186-1](https://doi.org/10.1016/S1359-6454(03)00186-1).
- [65] M. Masoumi, L.P.M. Santos, I.N. Bastos, S.S.M. Tavares, M.J.G. da Silva, H.F.G. de Abreu, Texture and grain boundary study in high strength Fe-18Ni-Co steel related to hydrogen embrittlement, *Mater. Des.* 91 (2016) 90–97, <https://doi.org/10.1016/j.matdes.2015.11.093>.
- [66] J.M. Rosenberg, H.R. Piehler, Calculation of the Taylor factor and lattice rotations for BCC metals deforming by pencil glide, *Metall. Trans.* 2 (1971) 257–259, <https://doi.org/10.1007/BF02662666>.
- [67] D. Raabe, Investigation of contribution of {123} slip planes to development of rolling textures in bcc metals by use of Taylor models, *Mater. Sci. Technol.* 11 (1995) 455–460.
- [68] S. Sodjit, V. Uthaisangskul, Microstructure based prediction of strain hardening behavior of dual phase steels, *Mater. Des.* 41 (2012) 370–379.
- [69] M. Masoumi, E.A. Ariza, A. Sinatara, H. Goldenstein, Role of crystallographic orientation and grain boundaries in fatigue crack propagation in used pearlitic rail steel, *Mater. Sci. Eng. A* 722 (2018) <https://doi.org/10.1016/j.msea.2018.03.028>.
- [70] D. De Knijf, E.P. Da Silva, C. Föjer, R. Petrov, Study of heat treatment parameters and kinetics of quenching and partitioning cycles, *Mater. Sci. Technol.* 0 (2014) <https://doi.org/10.1179/1743284714Y.00000007101743284714Y.000>.
- [71] G. Cheng, K.S. Choi, X. Hu, X. Sun, Determining individual phase properties in a multi-phase Q&P steel using multi-scale indentation tests, *Mater. Sci. Eng. A* (2015) 37–45, <https://doi.org/10.1016/j.msea.2015.11.072>.
- [72] J.B. Seol, D. Raabe, P.P. Choi, Y.R. Im, C.G. Park, Atomic scale effects of alloying, partitioning, solute drag and austempering on the mechanical properties of high-carbon bainitic-austenitic TRIP steels, *Acta Mater.* 60 (2012) 6183–6199, <https://doi.org/10.1016/j.actamat.2012.07.064>.
- [73] Z. Zribi, H. Houchin, F. Herbst, V. Optasanu, N. Njah, EBSD, XRD and SRS characterization of a casting Al-7wt% Si alloy processed by equal channel angular extrusion: dislocation density evaluation, *Mater. Charact.* 153 (2019) 190–198.
- [74] F.A.-F.W. Poling, V. Savic, H. Hector Jr., A.K. Sachdev, X. Hu, A. Devaraj, X. Sun, Combined synchrotron X-ray diffraction and digital image correlation technique for measurement of austenite transformation with strain in TRIP-assisted steels, *SAE Int* (2016) 1–5.
- [75] Y. Zou, Y.B. Xu, Z.P. Hu, X.L. Gu, F. Peng, X.D. Tan, S.Q. Chen, D.T. Han, R.D.K. Misra, G.D. Wang, Austenite stability and its effect on the toughness of a high strength ultra-low carbon medium manganese steel plate, *Mater. Sci. Eng. A* 675 (2016) 153–163, <https://doi.org/10.1016/j.msea.2016.07.104>.
- [76] R. Ding, D. Tang, A. Zhao, H. Guo, J. He, C. Zhi, Effect of ultragrain refinement on quenching and partitioning steels manufactured by a novel method, *Mater. Des.* 87 (2015) 640–649, <https://doi.org/10.1016/j.matdes.2015.08.073>.
- [77] C. Song, H. Yu, L. Li, T. Zhou, J. Lu, X. Liu, The stability of retained austenite at different locations during straining of I&Q&P steel, *Mater. Sci. Eng. A* 670 (2016) 326–334, <https://doi.org/10.1016/j.msea.2016.06.044>.
- [78] H.S. Zhao, W. Li, X. Zhu, X.H. Lu, L. Wang, S. Zhou, X.J. Jin, Analysis of the relationship between retained austenite locations and the deformation behavior of quenching and partitioning treated steels, *Mater. Sci. Eng. A* 649 (2015) 18–26, <https://doi.org/10.1016/j.msea.2015.09.088>.
- [79] C. Ghosh, C.J. Aranas, J.J. Jonas, Dynamic transformation of deformed austenite at temperatures above the Ae3, *Prog. Mater. Sci.* 82 (2016) 151–233, <https://doi.org/10.1016/j.pmatsci.2016.04.004>.
- [80] N.J. Petch, The cleavage strength of polycrystals, *J. Iron Steel Inst.* 173 (1953) 25–28.
- [81] E.O. Hall, The deformation and ageing of mild steel, *Proc. Phys. Soc. London Sect. B* 64 (1951) 747–753, <https://doi.org/10.1088/0370-1301/64/9/303>.
- [82] D. Wallis, L.N. Hansen, T. Ben Britton, A.J. Wilkinson, Geometrically necessary dislocation densities in olivine obtained using high-angular resolution electron

- backscatter diffraction, *Ultramicroscopy* 168 (2016) 34–45, <https://doi.org/10.1016/j.ultramicro.2016.06.002>.
- [83] T.J. Ruggles, Characterization of Geometrically Necessary Dislocation Content with EBSD-Based Continuum Dislocation Microscopy, Brigham Young University, 2015 <https://doi.org/10.1109/ETCS.2010.443>.
- [84] N.A. Fleck, M.F. Ashby, J.W. Hutchinson, The role of geometrically necessary dislocations in giving material strengthening, *Scr. Mater.* 48 (2003) 179–183, [https://doi.org/10.1016/S1359-6462\(02\)00338-X](https://doi.org/10.1016/S1359-6462(02)00338-X).
- [85] J. Jiang, T.B. Britton, A.J. Wilkinson, Measurement of geometrically necessary dislocation density with high resolution electron backscatter diffraction: effects of detector binning and step size, *Ultramicroscopy* 125 (2013) 1–9, <https://doi.org/10.1016/j.ultramicro.2012.11.003>.
- [86] H. Azzeddine, K. Tirsatine, T. Baudin, M.H. Mathon, A.L. Helbert, F. Brisset, D. Bradai, On the stored energy evolution after accumulative roll-bonding of invar alloy, *Mater. Chem. Phys.* 201 (2017) 408–415, <https://doi.org/10.1016/j.matchemphys.2017.08.063>.
- [87] C. Zheng, N. Xiao, L. Hao, D. Li, Y. Li, Numerical simulation of dynamic strain-induced austenite-ferrite transformation in a low carbon steel, *Acta Mater.* 57 (2009) 2956–2968, <https://doi.org/10.1016/j.actamat.2009.03.005>.
- [88] C. Garcia-Mateo, F.G. Caballero, C. Capdevila, C.G. De Andres, Estimation of dislocation density in bainitic microstructures using high-resolution dilatometry, *Scr. Mater.* 61 (2009) 855–858, <https://doi.org/10.1016/j.scriptamat.2009.07.013>.
- [89] M.J. Santofimia, C. Kwakernaak, W.G. Sloof, L. Zhao, J. Sietsma, Experimental study of the distribution of alloying elements after the formation of epitaxial ferrite upon cooling in a low-carbon steel, *Mater. Charact.* 61 (2010) 937–942, <https://doi.org/10.1016/j.matchar.2010.06.006>.
- [90] J. Wang, S. van der Zwaag, Stabilization mechanisms of retained austenite in transformation-induced plasticity steel, *Metall. Mater. Trans. A* 32 (2001) 1527–1539, <https://doi.org/10.1007/s11661-001-0240-5>.
- [91] J. Chiang, B. Lawrence, J.D. Boyd, A.K. Pilkey, Effect of microstructure on retained austenite stability and work hardening of TRIP steels, *Mater. Sci. Eng. A* 528 (2011) 4516–4521, <https://doi.org/10.1016/j.msea.2011.02.032>.
- [92] Y.F. Shen, L.N. Qiu, X. Sun, L. Zuo, P.K. Liaw, D. Raabe, Effects of retained austenite volume fraction, morphology, and carbon content on strength and ductility of nanostructured TRIP-assisted steels, *Mater. Sci. Eng. A* 636 (2015) 551–564, <https://doi.org/10.1016/j.msea.2015.04.030>.
- [93] R. Ding, D. Tang, A. Zhao, R. Dong, J. Cheng, X. Zhang, A new type of quenching and partitioning processing developed from martensitic pre-microstructure, *Mater. Manuf. Process.* 29 (2014) 704–709, <https://doi.org/10.1080/10426914.2014.912304>.
- [94] N. Nakada, Y. Ishibashi, T. Tsuchiyama, S. Takaki, Self-stabilization of untransformed austenite by hydrostatic pressure via martensitic transformation, *Acta Mater.* 110 (2016) 95–102, <https://doi.org/10.1016/j.actamat.2016.03.048>.
- [95] Y. Weng (Ed.), *Ultra-Fine Grained Steels*, Springer Berlin Heidelberg, Beijing, 2009.
- [96] R. Hielscher, D. Mainprice, H. Schaeben, Material behavior: texture and anisotropy, in: W. Freeden, M.Z. Nashed, T. Sonar (Eds.), *Handb. Geomathematics*, Second ed., 2010, Springer-Verlag Berlin Heidelberg 2010, pp. 2149–2188, https://doi.org/10.1007/978-3-642-54551-1_33.
- [97] P.A. Davies, M. Novovic, V. Randle, P. Bowen, Application of electron backscatter diffraction (EBSD) to fracture studies of ferritic steels, *J. Microsc.* 205 (2002) 278–284, <https://doi.org/10.1046/j.1365-2818.2002.00998.x>.
- [98] D. Hughes, L.N. Hansen, High angle boundaries formed by grain subdivision mechanisms, *Acta Mater.* 45 (1997) 3871–3886.
- [99] G.R. Ebrahimi, A. Momeni, H.R. Ezatpour, Modeling the viscoplastic behavior and grain size in a hot worked Nb-bearing high-Mn steel, *Mater. Sci. Eng. A* 714 (2018) 25–35.
- [100] M.J. Santofimia, L. Zhao, J. Sietsma, Microstructural evolution of a low-carbon steel during application of quenching and partitioning heat treatments after partial austenitization, *Metall. Mater. Trans. A Phys. Metall. Mater. Sci.* 40 (2009) 46–57, <https://doi.org/10.1007/s11661-008-9701-4>.
- [101] J. Zhang, H. Ding, R.D.K. Misra, C. Wang, Microstructural evolution and consequent strengthening through niobium-microalloying in a low carbon quenched and partitioned steel, *Mater. Sci. Eng. A* 641 (2015) 242–248, <https://doi.org/10.1016/j.msea.2015.06.050>.
- [102] S. Yan, X. Liu, W.J. Liu, T. Liang, B. Zhang, L. Liu, Y. Zhao, Comparative study on microstructure and mechanical properties of a C-Mn-Si steel treated by quenching and partitioning (Q&P) processes after a full and intercritical austenitization, *Mater. Sci. Eng. A* 684 (2017) 261–269, <https://doi.org/10.1016/j.msea.2016.12.026>.
- [103] S. Yan, X. Liu, W.J. Liu, H. Lan, H. Wu, Comparison on mechanical properties and microstructure of a C-Mn-Si steel treated by quenching and partitioning (Q&P) and quenching and tempering (Q&T) processes, *Mater. Sci. Eng. A* 620 (2014) 58–66, <https://doi.org/10.1016/j.msea.2014.09.047>.
- [104] W. Li, H. Gao, H. Nakashima, S. Hata, W. Tian, In-situ EBSD study of deformation behavior of retained austenite in a low-carbon quenching and partitioning steel via uniaxial tensile tests, *Mater. Charact.* 118 (2016) 431–437, <https://doi.org/10.1016/j.matchar.2016.06.020>.
- [105] Y. Lee, J.N. Kim, G. Kim, T. Lee, C.S. Lee, Improved cold-rollability of duplex light-weight steels utilizing deformation-induced ferritic transformation, *Mater. Sci. Eng. A* 742 (2019) 835–841, <https://doi.org/10.1016/j.msea.2018.11.043>.